Geophysical Journal International

Geophys. J. Int. (2016) **206,** 63–84
Advance Access publication 2016 April 6
GJI Seismology

doi: 10.1093/gji/ggw127

Numerical investigation of the seismic detectability of carbonate thin beds in the Boom Clay formation

José M. Carcione and Davide Gei

OGS, I-34010 Trieste, Italy. E-mail: jcarcione@ogs.trieste.it

Accepted 2016 April 1. Received 2016 April 1; in original form 2015 November 13

SUMMARY

The present study evaluates the capacity of the Boom Clay as a host rock for disposal purposes, more precisely its seismic characterization, which may assess its long-term performance to store radioactive wastes. Although the formation is relatively uniform and homogeneous, there are embedded thin layers of septaria (carbonates) that may affect the integrity of the Boom Clay. Therefore, it is essential to locate these geobodies. The seismic data to characterize the Boom Clay has been acquired at the Kruibeke test site. The inversion, which allowed us to obtain the anisotropy parameters and seismic velocities of the clay, is complemented with further information such as log and laboratory data. The attenuation properties have been estimated from equivalent formations (having similar composition and seismic velocities). The inversion yields quite consistent results although the symmetry of the medium is unusual but physically possible, since the anisotropy parameter ϵ is negative. According to a time-domain calculation of the energy velocity at four frequency bands up to 900 Hz, velocity increases with frequency, a behaviour described by the Zener model. Then, we use this model to describe anisotropy and anelasticity that are implemented into the equation of motion to compute synthetic seismograms in the space–time domain. The technique is based on memory variables and the Fourier pseudospectral method. We have computed reflection coefficients of the septaria thin layer. At normal incidence, the *P*-wave coefficient vanishes at specific thicknesses of the layer and there is no conversion to the *S* wave. For example, calculations at 600 Hz show that for thicknesses of 1 m the septarium can be detected more easily since the amplitudes are higher (nearly 0.8). Converted *PS* waves have a high amplitude at large offsets (between 30° and 80°) and can be useful to identify the target on this basis. Moreover, we have investigated the effect of septaria embedded in the Boom Clay with several simulations, by considering a lateral partial continuity of the calcareous thin inclusions. The simulations with layers of calcareous material show continuity of the reflections even when the percentage of carbonate within the layer is very small (5–15 per cent), while for low content of the calcareous material, isolated septaria boulders generate diffraction events. We have also simulated the stacked seismic section obtained from processing of the field data. The matching between the field and synthetic sections is acceptable.

Key words: Elasticity and anelasticity; Seismic anisotropy; Seismic attenuation.

1 INTRODUCTION

The safe disposal of nuclear waste is a challenge and geological disposal seems to be the most preferred solution. Non-intrusive seismic methods are suitable techniques to characterize subsurface waste repository sites and monitor their evolution (Marelli *et al.* 2010; Zhang & Juhlin 2014). A candidate geological site in Belgium is the Rupel Clay formation, commonly called the Boom Clay, composed of clays that at the top and base are more silty and have embedded thin layers of septaria (according to the Merriam Webster dictionary, a septarium is *a concretionary nodule usually of limestone or clay ironstone intersected within by cracks filled with calcite, barite, or other minerals*). Silt and clay thin layers behave as fine layering at seismic frequencies inducing effective anisotropy (e.g. Vandenberghe 1978). The septaria are fractured stiff concretions, stiffer than the clay. Water flows preferentially along the septaria layers, as can be inferred from outcrops in Belgium. These outcrops show that the septaria have elongated and flat spheroidal shapes with their axes parallel to the bedding planes of the clay, that is, horizontally oriented. The formation of this concretions (lithification) started early in the diagenesis process near the sediment-water interface and before compaction occurred (De Craen *et al.* 2004).

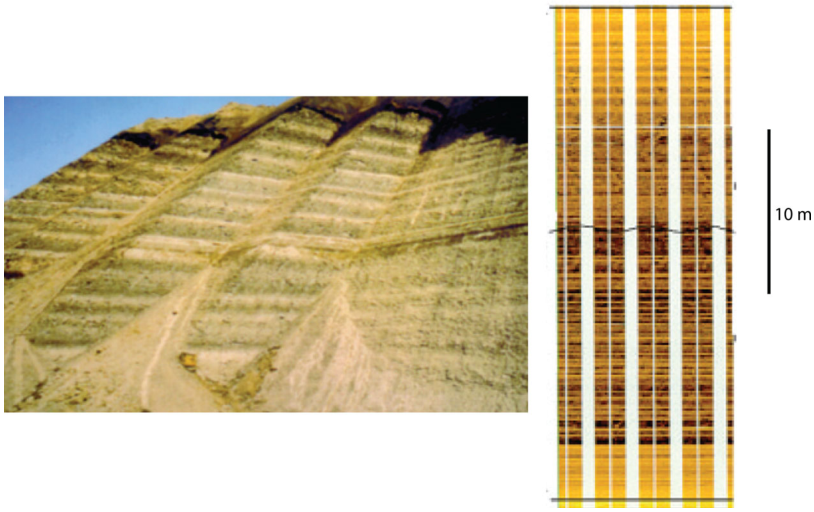

Figure 1. Outcrop (left) and high-resolution formation-microimager log (HADES site) (right) showing the bedding of the Boom Clay (from Wouters & Vandenberghe 1994) (see also Abels *et al.* 2007; Vanderberghe *et al.* 2014).

Due to the high permeability, these septaria layers may constitute a problem regarding the integrity of the Boom Clay. Therefore, it is essential to locate these geobodies.

The modelling study presented here addresses the seismic characterization of the Boom Clay with the presence of geobodies (layers and septaria), its diffractions at vertical-seismic-profile (VSP) and surface-data resolutions, including velocity anisotropy and angle-dependent amplitude to obtain a proper image of the geobodies. Any rigorous seismic study requires the characterization of the background formation. Well logs, laboratory experiments and existing seismic data are used to determine the velocity and attenuation anisotropy of the Boom Clay. As a first approximation, we consider an homogeneous medium obtained with the five deeper shots of a reverse vertical-seismic-profile (RVSP) data set (Eddies 2014). The direct arrivals from these shots show that the medium has a vertical velocity higher than the horizontal velocity.

A velocity-dispersion analysis based on four frequency bands up to 900 Hz indicates that the wave velocity increases with frequency. This behaviour is properly described by the Zener model. Then, we use a Zener-type stress–strain relation to describe anisotropy and anelasticity. A suitable model describes the Boom Clay as a transversely isotropic (TI) medium including seismic loss, which can be used for the computation of numerical wavefields in inhomogeneous media (Carcione 2015). Moreover, we calculate the reflection coefficients (pre- and post-critical) of thin layers of carbonates embedded in the clay and verify if post-critical information can be useful to estimate the presence and location of the septaria.

We then define geological models based on well logs, seismic and geological data, consisting of thin layers of carbonates and boulders (septaria), in order to compute synthetic seismograms (RVSPs and surface seismic) with a full-wave solver, based on the Fourier pseudospectral method, and different types of sources and receiver configurations (Carcione 1999, 2015) to assess the seismic visibility of the septaria as thin layers and as isolated geobodies. These simulations can be used to determine optimal acquisition parameters and locate these geobodies through the analysis of diffractions (inversion and/or seismic migration). Moreover, the synthetic seismograms can be used to verify the performance of existing inversion or processing algorithms before their application to real data.

2 MODEL PROPERTY DETERMINATION

In this section, we characterize the Boom Clay as an anisotropic and viscoelastic medium to describe seismic velocity and attenuation variations with the propagation direction. The clay is highly anisotropic as can be seen in Fig. 1, where an outcrop and FMI log are shown. Bedding induces seismic anisotropy, since the wavelength of seismic waves is much larger than the thickness of the single layers. This is termed effective anisotropy (e.g. Carcione 2015). Data about seismic anisotropy of the Boom Clay are scarce if not absent. Elastic constants, measured on cores by Piriyakul (2006), are taken as a reference and corrected by field measurements from Eddies (2014), reprocessed as indicated below.

2.1 Elasticity constants from laboratory experiments

Laboratory data to calibrate the seismic model are scarce and partially contradict the seismic experiments. We attempt to reconcile them, but give priority to the available seismic data. The degree of velocity anisotropy of the Boom Clay has been estimated by Piriyakul (2006), who made experiments on samples collected down to 10 m depth. The undisturbed Boom clay is sampled at the research site Sint-Katelijne-Waver in Belgium, where there is an outcrop. Reconstituted Boom clay samples are made at the same void ratio and natural water content of the undisturbed sample. Two prototype triaxial apparatuses are used to investigate the small strain anisotropic stiffness of the Boom clay incorporating both multi-directional bender element and local strain measurements. Appendix A reports Piriyakul's relevant equations to deal with this problem. The confining and pore pressures at depth z are $p_c = \bar{\rho} g z$ and $p_H = \rho_w g z$, where $\bar{\rho}$ is the average sediment density, ρ_w is the water density and $g = 9.81$ m s^{-2}. For $\bar{\rho} = 1.8$ g cm^{-3}, $\rho_w = 1$ g cm^{-3} and $z = 50$ m (the maximum depth of the Kruibeke data), we have an effective pressure $p_e = p_c - p_H = 392$ kPa. The data are taken from table 6.5 of Piriyakul (2006) (test at 400 kPa effective pressure), where $G_{hh} = F_h(1 - \nu_{hh})/(1 + \nu_{hh})/2 = 1/s_{66}$ in that thesis, where F_h is the horizontal stiffness modulus. Hence, this test is the one that more approximates the *in-situ* conditions considered here. The results are

$$c_{11} = 0.64 \text{ GPa}, \quad c_{13} = 0, \quad c_{33} = 0.28 \text{ GPa},$$
$$c_{55} = 0.15 \text{ GPa}, \quad c_{66} = 0.31 \text{ GPa}.$$

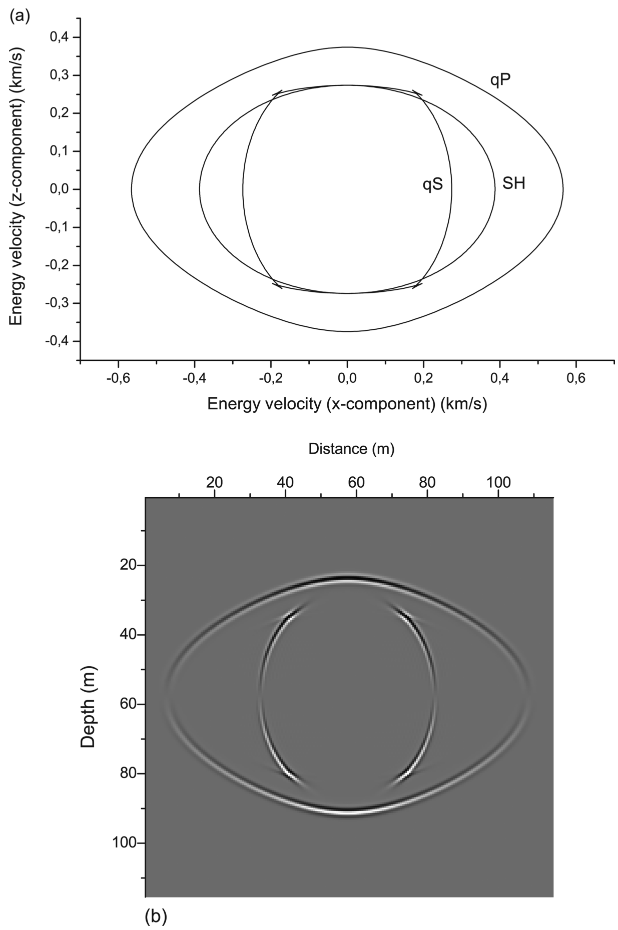

Figure 2. Energy (ray) velocity (a) and snapshot (b) of the wave propagating in Boom Clay (from laboratory data; Piriyakul 2006). The centre frequency of the source is 140 Hz.

Then, Thomsen anisotropy parameters (see Appendix A) are $\epsilon = 0.6$, $\gamma = 0.5$, $\delta = 0.12$ and $v_P/v_S = \sqrt{c_{33}/c_{55}} = 1.34$, where v_P and v_S are *P*- and *S*-wave velocities along the vertical direction. Fig. 2 shows the energy velocity (wave fronts) and a full-wave simulation (see below for the algorithm), where we assume a medium density $\rho = 2$ g cm^{-3}.

According to the Kruibeke test site (Eddies 2014), the characteristic *P*-wave velocity of the Boom Clay lies between $v_P = 1600$ m s^{-1} and $v_P = 1800$ m s^{-1}, while a (presumably) tube-wave velocity reported is $v_T = 374$ m s^{-1}. The tube wave is probably generated at a discontinuity identified as a partially saturated–fully saturated sediment interface at nearly 20 m due to rising of high-pressure water after drilling (see fig. 5.4.3 in Eddies 2014). Another possible cause of the generation of the tube wave is a discontinuity in the borehole properties, such as a broken PVC casing.

The *S*-wave velocity of the Boom Clay can be obtained as

$$v_S = \left[\rho\left(\frac{1}{\rho_w v_T^2} - \frac{1}{K_w}\right)\right]^{-1/2} \tag{1}$$

(White 1965; Carcione *et al.* 2008; Carcione 2015), where K_w is water bulk modulus and ρ is the mass density of the formation, the Boom Clay in this case. For $K_w = 2.25$ GPa and $\rho = 2$ g cm^{-3}, we obtain $v_S = 273$ m s^{-1}. This value is close to that measured by Piriyakul (2006) (278 m s^{-1}), while the Piriyakul *P*-wave velocity (374 m s^{-1}) greatly differs from the value obtained in Eddies (2014). However, the *S*-wave velocity obtained from the tube wave is probably too low due to hole alteration (unconsolidation due to drilling) and we should expect a higher value, also for stability (physical realizability) reasons as we shall see below.

Table 1. *P*-wave arrival time inversion of the five deeper shots from the RVSP experiment.

Shot #	Source depth (m)	v_P (m s^{-1})	ϵ	δ
48	44	1624	−0.039	0.231
49	45	1635	−0.024	0.182
50	46	1639	−0.020	0.174
51	47	1639	−0.025	0.171
52	48	1648	−0.039	0.153

2.2 *P*-wave traveltime inversion of RVSP data

Conventional seismic-data processing and interpretation are based on the hyperbolic approximation of the moveout, as a consequence of the assumption of an isotropic subsoil. These techniques become inaccurate when anisotropic data are processed under the assumption of isotropy (e.g. Lynn *et al.* 1991; Tsvankin 2012). Anisotropy significantly affects the normal-moveout velocity (NMO) and must be considered in the process of characterization. A relatively simple but effective method to quantify anisotropy from seismic data is the inversion of *P*-wave arrival times. Traditionally used for active seismic applications (Alkhalifah & Tsvankin 1995; Grechka & Tsvankin 1998), the inversion can also be applied to microseismic and RVSP data (Gei *et al.* 2011). We assume that the shale, approximated as a single homogeneous VTI medium (vertical symmetry axis), is equivalent to a medium formed with isotropic or anisotropic thin layers (Backus 1962; Grechka & Tsvankin 1998). The reliability of these methods depends on the maximum offset of the seismic data as the non-hyperbolicity occurs at large source–receiver distances. RVSP data have an offset-to-source-depth ratio of 1.5. This unusual high value makes this kind of inversion particularly suitable for this data set.

We consider Eddie's RVSP data (Eddie 2014) and invert for ϵ and δ of the effective medium representing the Boom Clay. It is well known that RVSP and VSP data are more reliable than surface data. The acquisition configuration uses a sparker source in a well and hydrophones at the surface located in a trench filled with water. RVSP experiments have the ideal geometry for the inversion method described in Appendix B. The method is based on the traveltime approximation proposed by Alkhalifah & Tsvankin (1995) for reflected waves but the formulation is still valid for direct waves (Gei 2013). We inverted the five deeper shots from the RVSP data set of the Boom Clay and the results are summarized in Table 1 (see also Fig. 3b). The average values of the anisotropy parameters are $\epsilon = -0.0294$ and $\delta = 0.182$. The average value of the vertical velocity is 1637 m s^{-1}. While ϵ is negative and differs from that of Piriyakul (2006), δ has a similar value. Negative ϵ is possible in finely layered media, with a minimum value of −3/8 for two isotropic thin layers with equal spatial frequency (Berryman *et al.* 1999).

2.2.1 *Seismic elasticity constants*

Taking the *P*-wave velocity obtained from inversion of RVSP arrival times (1637 m s^{-1}) and the *S*-wave velocity computed from the tube wave (273 m s^{-1}), we have $c_{33} = \rho v_P^2$ and $c_{55} = \rho v_S^2$, giving the

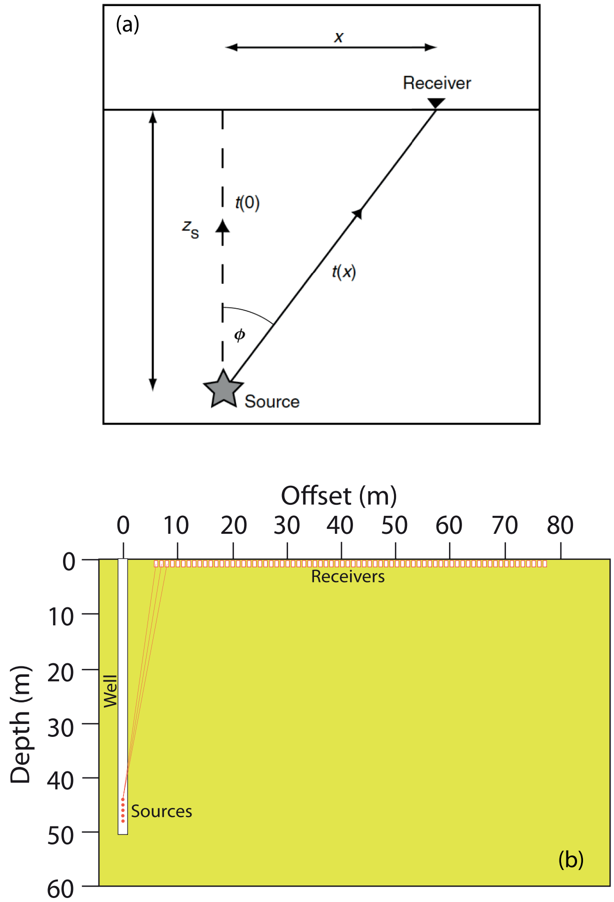

Figure 3. (a) Schematic representation of a RVSP experiment; x is the receiver offset and ϕ is the dip angle (after Gei *et al.* 2011). (b) RVSP data to obtain the properties of the Boom Clay (five shots are shown).

following elasticity constants

$$c_{11} = 5.04 \text{ GPa}, \quad c_{13} = 5.96 \text{ GPa}, \quad c_{33} = 5.36 \text{ GPa},$$
$$c_{55} = 0.15 \text{ GPa}, \quad c_{66} = 0.3 \text{ GPa}, \quad c_{12} = 4.44 \text{ GPa}. \tag{2}$$

Basically, any real medium must satisfy a set of stability conditions. These are given in Appendix C for a TI medium. The medium represented by eq. (2) violates the second equation (C1), even for $c_{66} = c_{55}$. Hence, the medium is physically non-realizable and cannot exist in nature. Although eq. (1) is a low-frequency approximation and the tube-wave velocity is measured at 150 Hz approximately, this discrepancy is not the cause of the violation of the stability condition, since the velocity dispersion is too small.

Therefore, we choose the minimum S-wave velocity such that the medium is physically stable, which occurs for $v_S = \sqrt{c_{55}/\rho} =$ 730 m s^{-1}. This value is consistent with S-wave velocities obtained by Neerdael *et al.* (1992) from seismic experiments; see their fig. 10, where $v_P = 1650$ m s^{-1} and $v_S = 730$ m s^{-1} are reported. Since the purpose here is to obtain the seismic properties obtained from the inversion of the RVSP traveltimes, we consider $v_P =$ 1637 m s^{-1}, $v_S = 730$ m s^{-1}, $\epsilon = -0.0294$, $\gamma = 0$, $\delta = 0.182$ and $\rho = 2$ g cm^{-3}, where the value of γ reflects the fact that we have no information about the S-wave velocity from Eddies (2014) and therefore we assume the simplest scenario, that is, SH-wave isotropy. The assumed P-wave velocity of the Boom Clay is consistent with the fact that the base of this formation is located at approximately 50 m depth in Eddies (2014) (see their model at page 26).

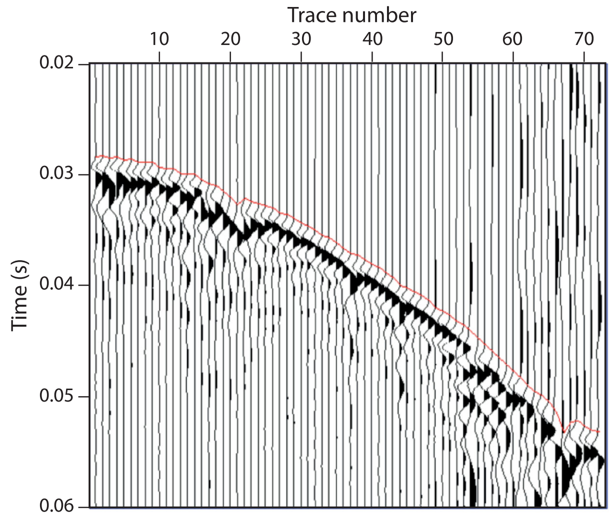

Figure 4. Picking of the shot 52 (deepest source of the data set: 48 m).

With this choice, we finally obtain

$$c_{11} = 5.04 \text{ GPa}, \quad c_{13} = 4.11 \text{ GPa}, \quad c_{33} = 5.36 \text{ GPa},$$
$$c_{55} = 1.06 \text{ GPa}, \quad c_{66} = 1.06 \text{ GPa}, \quad c_{12} = 2.91 \text{ GPa}, \tag{3}$$

which gives a P-wave velocity $v_P = \sqrt{c_{11}/\rho} = 1588$ m s^{-1} along the horizontal direction. This characterization is the best that agrees with the RVSP data, which are the most reliable data, and it is clear that to honour the data, anisotropy has to be considered, as well as attenuation, as we shall see below.

2.2.2 *Modelling verification*

We have checked the effectiveness of the inversion by performing numerical simulations with the parameters given in Table 1 and compared the picked arrival times of the synthetic data with the arrival times obtained from the experimental data. The synthetic data are computed with a full-wave method (no approximations). The 2-D wave equation is numerically solved with a Fourier method and the time integration is based on a fourth-order Runge–Kutta scheme. A complete description of the modelling algorithm can be found in chapter 9 of Carcione (2015).

Fig. 4 shows the picking of first breaks of shot 52 with the source located at 48 m depth. This is the deepest source point in the RVSP data set, while Fig. 5 displays the arrival times picked from the seismograms of shots 48–52. Fig. 6 shows the synthetic seismogram computed with the geometry of shot 52 and the seismic properties given in Table 2. The red line represents the picking of the first break (arrival time). The arrival times of the field and synthetic data are shown in Fig. 7. The good matching of these two data sets confirms the effectiveness of the inversion technique to compute the anisotropy parameters. The comparison of the field and synthetic arrival times with theoretical arrival times for an isotropic medium (green crosses) proves the anisotropic character of the Boom Clay.

We have obtained similar results for shots 48–51. Fig. 8 shows the difference between the synthetic and the experimental arrival times of the five RVSP shots analysed in this study. These time differences are quite consistent with each other and most of the samples are confined in the range ± 0.5 ms, which makes the inversion results quite reliable.

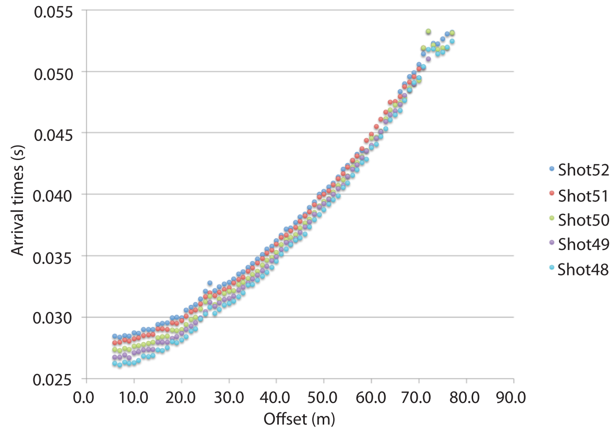

Figure 5. Arrival times picked from the seismograms of the shots 48–52 of the RVSP data set.

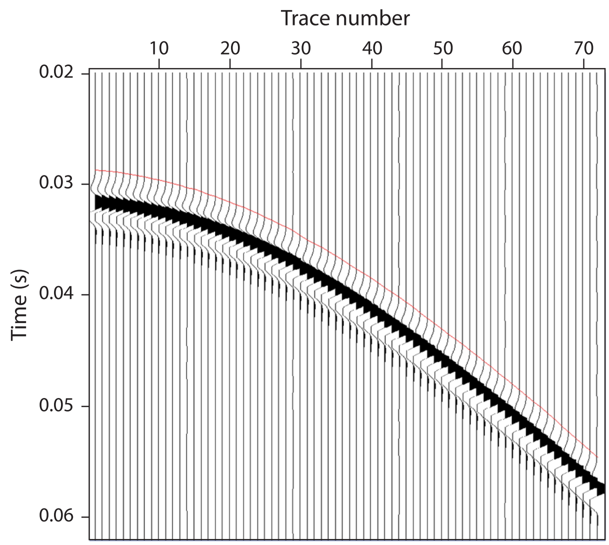

Figure 6. Synthetic seismograms reproducing the experimental data of shot 52.

2.3 Estimation of the quality factor

The c_{IJ} obtained above correspond to the unrelaxed-high frequency-elastic values. This is due to the assumption that waves in elastic (lossless) media travel faster than waves in anelastic (lossy) media. In order to find the complex and frequency-dependent stiffness components, p_{IJ}, we require an estimation of the attenuation or quality factor of the P and S waves. Eddies (2014) estimated a P-wave quality factor of 10 from VSP data, which he considers not reliable and in disagreement with values reported for clays. Here, we consider values of Q measured for Pierre Shale (Carcione 2015), which is a formation as shallow as the Boom Clay. Attenuation measurements in a relatively homogeneous medium (Pierre Shale) were made by McDonal *et al.* (1958) near Limon, Colorado. They report a constant-Q behaviour up to 500 Hz, with attenuation factor

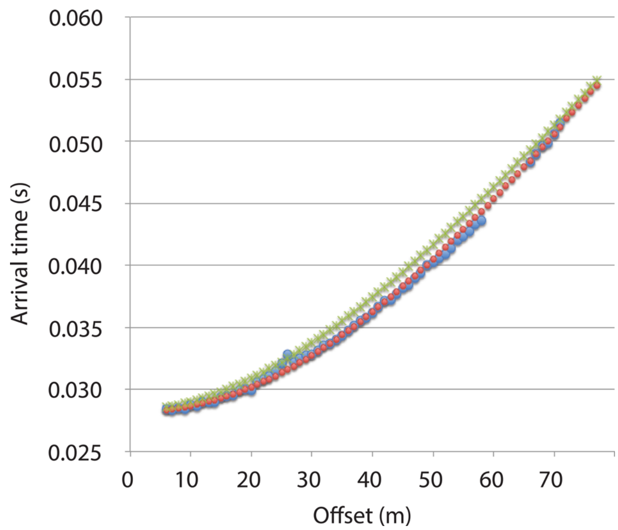

Figure 7. Experimental arrival times (blue) from shot 52, arrival times from full-wave modelling using the parameters of Table 1 (red) and theoretical arrival times for an isotropic medium (green) using the velocity given in Table 1.

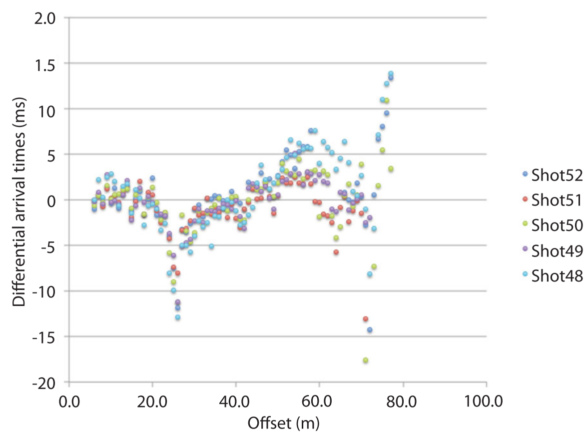

Figure 8. Difference between the synthetic and experimental arrival times for shots 48–52 of the RVSP data set.

given by: $\alpha_P = 0.12f$ and $\alpha_S = 1.0f$, where α is given in dB per 1000 ft and the frequency f in Hz. Conversion of units implies α (dB/1000 ft) = 8.686 α (neper/ 1000 ft) = 2.6475 α (neper km^{-1}). For low-loss solids, the quality factor is, according to Carcione (2015),

$$Q = \frac{\pi f}{\alpha v},$$

with α given in neper per unit length. Since v_P and v_S are approximately 7000 ft s^{-1} (2135 m s^{-1}) and 2630 ft s^{-1} (802 m s^{-1}), the P- and S-wave quality factors are $Q_P \simeq 32$ and $Q_S \simeq 10$. Generally, the higher the velocity the higher the quality factor and the lower the attenuation. This is because stiffer media have lower wave

Table 2. Material Properties.

Medium	v_P (m s^{-1})	v_S (m s^{-1})	ϵ	δ	Q_1 (Q_K)	Q_2 (Q_S)	ρ (g cm^{-3})
Boom Clay	1637	730	−0.029	0.182	30	10	2
Septaria	4385	2773	0	0	∞	∞	2.6

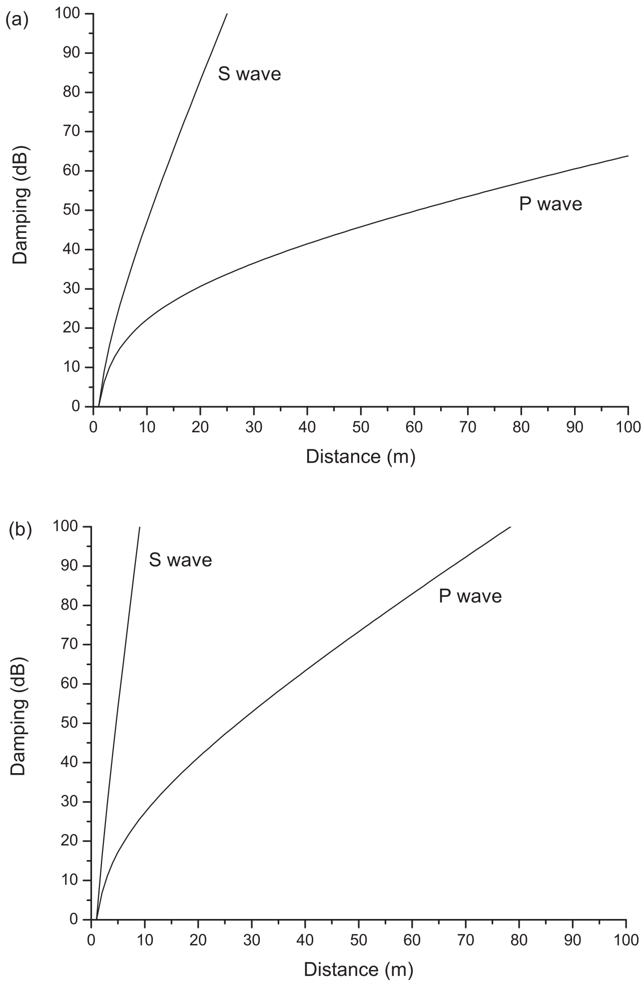

Figure 9. Damping factor as a function of distance for 300 Hz (a) and 1000 Hz (b) ($Q_P = 20$ and $Q_S = 10$).

attenuation, for example, granite has a lower attenuation than porous sandstone. The *P*-wave value of Pierre Shale is presumably an upper limit for the Boom Clay which has a lower velocity and if we consider higher frequencies (higher than 500 Hz), attenuation should be even stronger. Hence, a value of $Q_P = 20$ seems to be quite realistic. Pierre Shale has an *S*-wave velocity comparable to that of Boom Clay. This means that its Q_S is appropriate for Boom Clay. Summarizing, we assume $Q_P = 20$ and $Q_S = 10$. Neerdael *et al.* (1992) report a value of $Q_P = 7$ for the Boom Clay (see their fig. 8).

The damping factor in 3-D homogeneous media is given by

$$D = \frac{\exp(-\alpha r)}{r} = \frac{1}{r}\exp\left(-\frac{\pi f}{vQ}r\right) \quad (4)$$

where r is the distance travelled by the wave. The factor r^{-1} corresponds to the geometrical spreading, while the exponential describes the intrinsic attenuation. This expression gives a rough estimation of the damping. Fig. 9 shows the absolute value of the damping factors in dB units as

$$20\log_{10}\left(\frac{D}{D_0}\right), \quad (5)$$

where D_0 is the value of D at $r = 1$ m.

The dynamic range of the Geode system used in Eddies (2014) is 144 dB (system) and 110 dB (instantaneous) and the DHA-7 hydrophones have a sensitivity of 197 dB. Therefore, according to these values and Fig. 9, these systems can record *P*-wave signals travelling up to 100 m, while in principle shear wave can only be acquired at much shorter distances.

2.4 Anisotropy of velocity and attenuation

We have performed a frequency filtering of the data in four reliable frequency bands to analyse the velocity dispersion. The corner frequencies used for the trapezoidal frequency bandpass filtering are [0,50–250,280], [200,250–450,480], [400,450–650,680] and [600,650–850,880] (in Hz). As can be seen in Fig. 10, the events become noisy and 'ringy' at high frequencies. Then, if u is the recorded wavefield, we compute the arrival times at each band as the barycentre (centroid) of the energy field $|u|^2$, a method that has proved to be reliable in anisotropic viscoelastic media (see fig 3 in Carcione *et al.* 1996). The results are shown in Fig. 10, where it can be seen that higher frequencies travel with higher velocities. This behaviour is consistent with observations of—positive—velocity dispersion in the Earth and consistent with usual anelastic kernels—such as the Zener model—to describe seismic wave propagation (e.g. Carcione 2015). It is important to point out that the case of negative dispersion is possible in some situations, for instance in porous media, and can be explained as interference between the *P* wave and the slow—Biot—wave (e.g. Marutyan *et al.* 2006). This possibility has to be investigated by acquiring seismic data with better signal-to-noise ratio.

The model for velocity and attenuation anisotropy is based on a stress–strain relation given in Carcione (2015, chapter 4, model 3). We consider two independent (Zener) complex moduli, M_1 and M_2, to describe the attenuation kernels, determined by the Q_ν loss parameters. The expression of the complex moduli is given in eq. (4.6) of Carcione (2015). In this stress–strain relation, the mean stress (i.e. the trace of the stress tensor) is only affected by the dilatational complex modulus M_1, while the deviatoric-stress components solely depend on the shear complex moduli M_2. The trace of the stress tensor is invariant under transformations of the coordinate system. This fact assures that the mean stress depends only on M_1 in any system. While $Q_2 = Q_S$, to retrieve Q_1 requires some calculations. Since M_1 corresponds to dilatational deformations related to the bulk modulus K and not the *P*-wave modulus, we obtain Q_1 as indicated in Appendix D. From $Q_P = 20$, $Q_2 = Q_S = 10$, $v_P = 1637$ km s^{-1} and $v_S = 730$ m s^{-1}, we obtain $Q_1 = 30$. As mentioned above these values are consistent with those of the Pierre Shale and data published in the literature.

Summarizing, we consider the unrelaxed elasticity constants (3) and obtain the complex stiffnesses $p_{11} = (4.78, 0.25)$, $p_{13} = (4.06, 0.05)$, $p_{33} = (5.09, 0.25)$, $p_{55} = (0.96, 0.10)$, and $p_{66} = (0.96, 0.10)$ (values in GPa), where the frequency at which these stiffness components are reported corresponds to the peak of the Zener mechanism.

Appendix E provides the seismic properties of the anisotropic viscoelastic medium. Fig. 11 shows the energy (ray) velocity (a), attenuation factor (b) and quality factor (c) of the wave propagating in Boom Clay. The frequency is that of the relaxation peak. As expected, the horizontal *P*-wave velocity is smaller than the vertical *P*-wave velocity and strong anisotropy characterizes the qS wave, due to its coupling with the qP wave, while the *SH* wave shows isotropy because it is a pure mode and because Thomsen anisotropy parameter $\gamma = 0$. The qS wave has cuspidal triangles and the clay shows strong shear-wave splitting at most propagation directions (Carcione 2015).

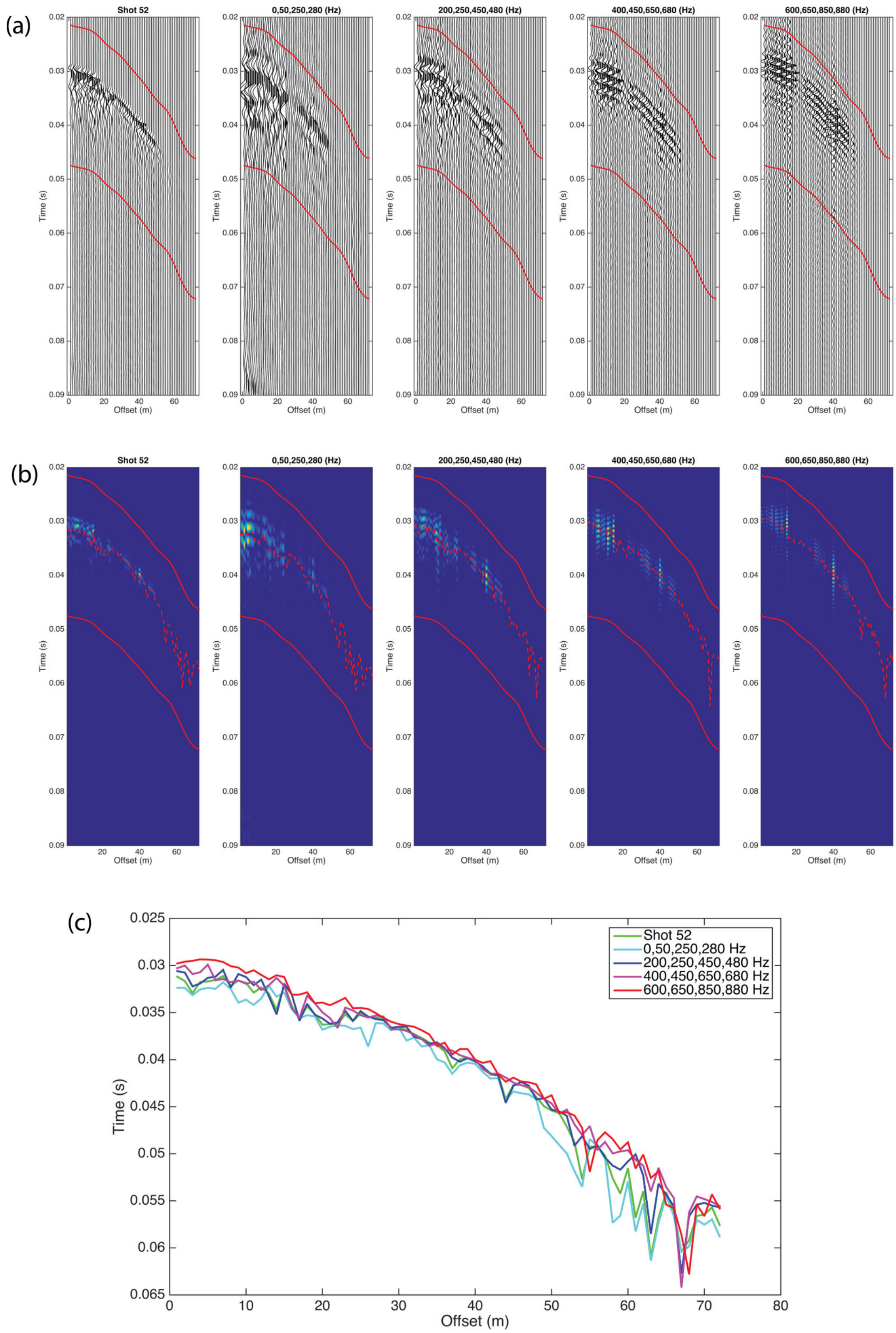

Figure 10. The panels show the seismic field (a), energy field (b) and traveltime as a function of offset (c) of shot 52 at four frequency bands. The continuous lines in panels (a) and (b) represent the time window use to compute the energy field and the dashed line in panel (b) represents the barycentre of the energy field.

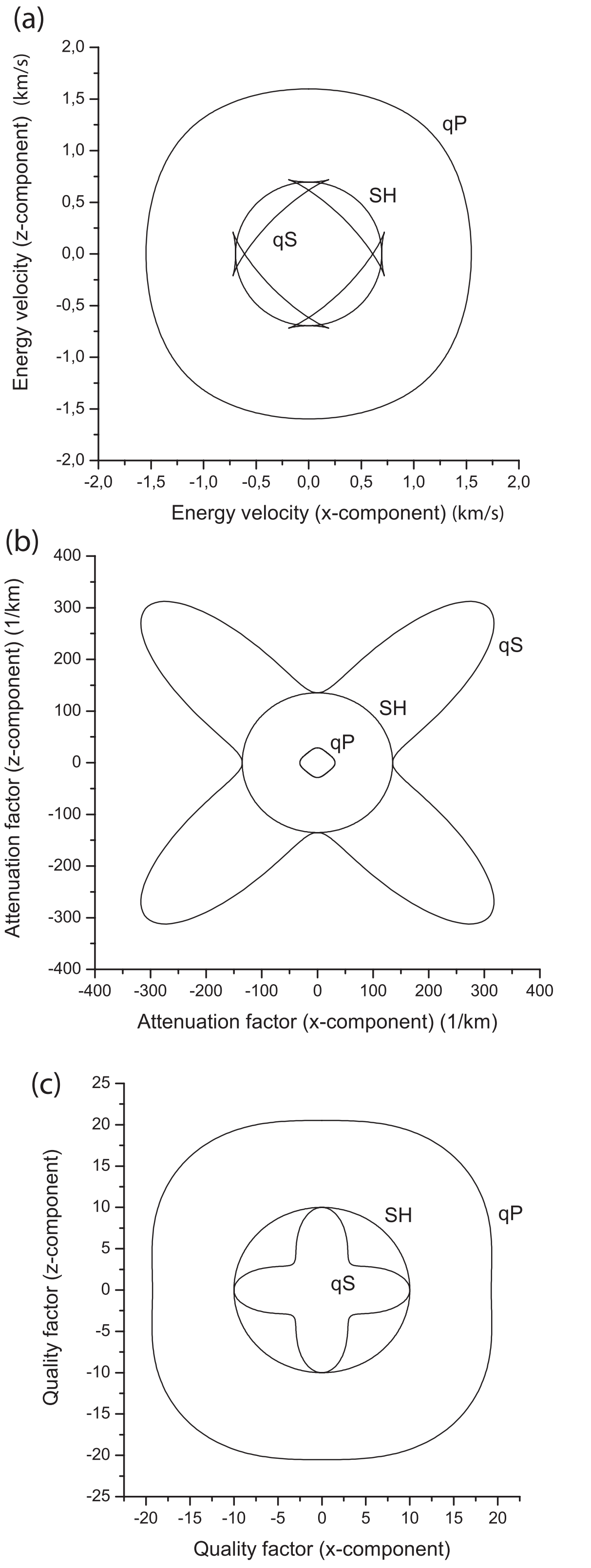

Figure 11. Energy (ray) velocity (a), attenuation factor (b) and quality factor (c) of the wave propagating in Boom Clay.

Figure 12. A calcareous septarium embedded in Boom Clay. The width is approximately 60 cm (from Vis & Verweij 2014).

3 SENSITIVITY AND DETECTABILITY ANALYSIS

3.1 Reflection coefficients and AVO analysis

A singular characteristic in the Boom Clay member is the presence of several thin layers made of ellipsoidal-shaped carbonate concretions, called septarium (if one) or septaria, whose sizes range from a few decimetres up to a couple of metres (see Figs 12 and 13). The seismic response of these thin layers is characterized by a set of parallel reflection events, which, depending on the frequency bandwidth, look like continuous horizontal events or alignments of diffraction events (Fig. 14) (see Vandenberghe 1978; Hemerijckx *et al.* 1983, his fig. 2). At low frequencies whose related wavelengths are much larger than the size of the carbonate layers and separation between the septaria geobodies, we may obtain the reflection coefficient and AVO response of these layers by representing the system as in Fig. 15.

We consider here the properties $v_{P1} = 1637$ m s^{-1}, $v_{S1} =$ 730 m s^{-1} and $\rho_1 = 2$ g cm^{-3} (clay) and $v_{P2} = 4385$ m s^{-1}, $v_{S2} =$ 2773 m s^{-1}, $\rho_2 = 2.6$ g cm^{-3} (carbonate) (Mavko *et al.* 2009). First, we compute the reflection coefficients at normal incidence and at 20° as a function of the thickness of the carbonate layer. Fig. 16 shows these coefficients for a frequency of 300 Hz. At normal incidence (a), the coefficient vanishes at the thicknesses indicated in Appendix F and there is no conversion to the *S* wave. At 20°, the conversion is remarkable and maximum PP coefficients occur for thicknesses between 3 and 5 m.

Fig. 17 shows similar plots for 600 Hz. In this case, thicknesses of 1 m can be detected more easily since the amplitudes are higher (nearly 0.8). Converted PS energy offers an additional possibility to detect the carbonate layers, since the *S*-wave energy shows a maximum where the *P*-wave energy is weak, for instance at 4 m thickness in Fig. 17(b). Then, it is recommended to perform AVO studies on both PP and PS events to avoid ambiguities in the interpretation.

Next, we represent the reflection coefficients as a function of the incidence angle. The expression (F2) given in Appendix F is an acoustic approximation, since it neglects the conversion of *P*-wave energy to shear motion. This expression is mainly used in exploration seismics. Fig. 18 shows the real part of $R_{\rm PP}$ (solid line) as a function of the incidence angle, compared to expression (F2) (dashed line) at a frequency $f = 300$ Hz and a layer thickness $h =$ 0.5 m (a) and $h = 1$ m (b), where we have considered the lossless case. Since ω and h always appear in the equations as ωh, the

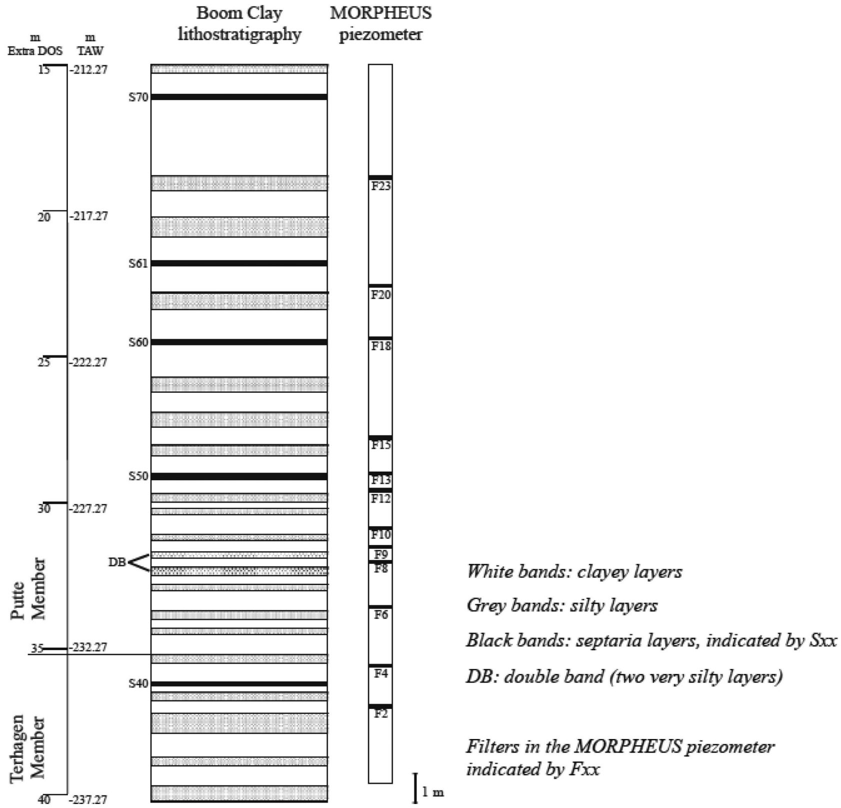

Figure 13. View of the MORPHEUS piezometer and its relative positioning towards the Boom Clay layering (from De Craen *et al.* 2004). Septaria represented as thin layers (black).

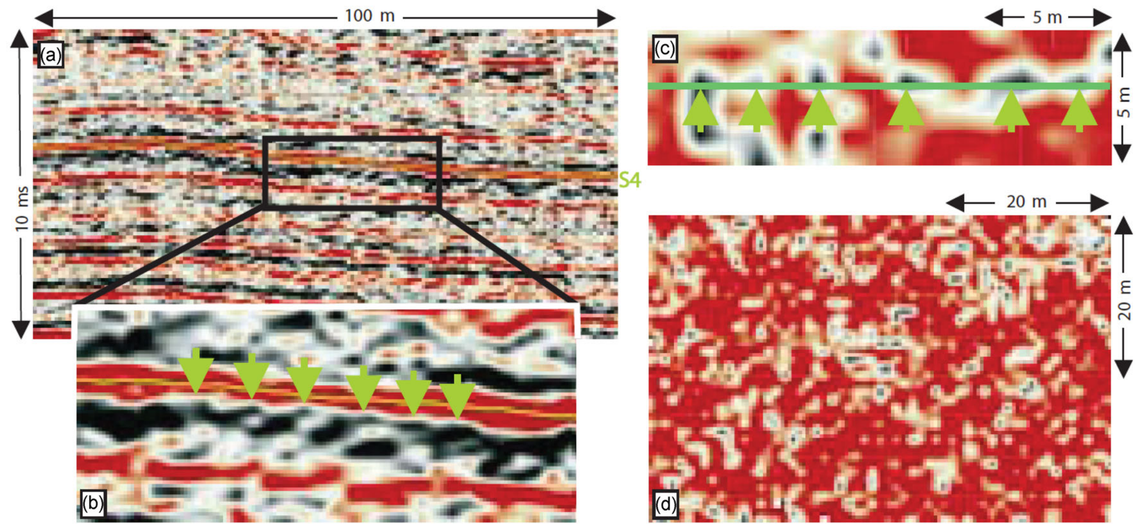

Figure 14. (a) In-line section showing a septaria level. (b) Close-up with single diffraction events. (c) Horizon slice at 0.2 ms below that level; the green arrows refer to events identified in (b). (d) Enlarged section showing typical blotchy pattern possibly suggesting concretion distribution (from Missiaen *et al.* 2002).

solution for $f = 300$ Hz and $h = 0.5$ m is the same as that for $f = 150$ Hz and $h = 1$ m. A transition angle at nearly 30° implies a notable variation at large offsets. Converted PS waves have a high amplitude at large offsets (between 30° and 80°) and can be useful to identify the target on this basis.

The oscillatory character of the curves implies an ambiguity of the coefficients with respect to the layer thickness because two or more values of h may correspond to the same value of the reflection coefficient. The period of the oscillations depends on the frequency, the layer thickness, and the wave velocity. For instance, minimum values of the PP-reflection coefficients are obtained by setting $\omega v_{\rm ph}/h = \pi$, where $v_{\rm ph}$ is the average phase velocity of the *P*-wave in the layer along the refracted ray (e.g. Carcione 2015, section 6.4). For increasing (decreasing) frequencies, the period of the oscillations decreases (increases). In practice, however, this ambiguity can be solved, since for a layer thickness greater than, say, $\pi v_{\rm ph}/2\omega_0$, the top and bottom seismic events can be resolved.

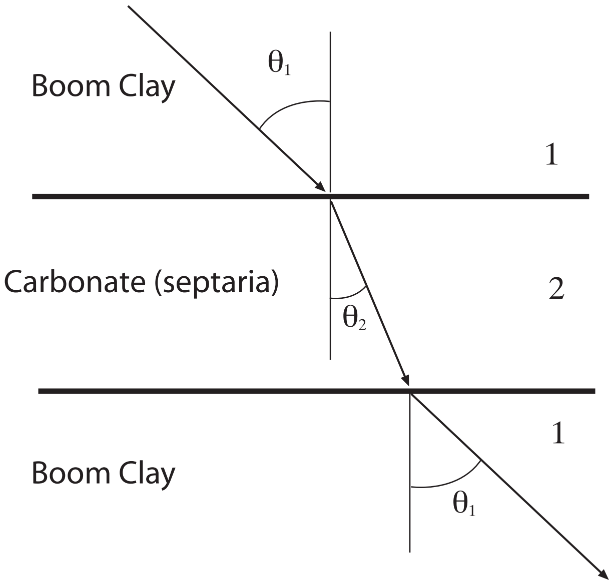

Figure 15. Thin carbonate layer (septaria) embedded in the Boom Clay. Ray representation of a plane wave propagating through a layer.

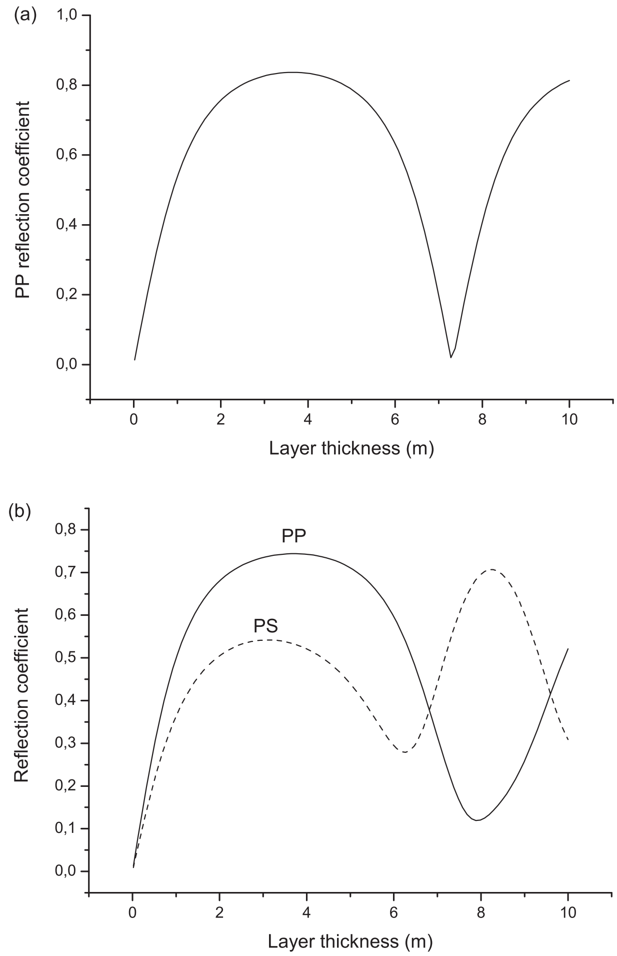

Figure 16. Reflection coefficients at normal incidence (a) and at 20° (b) as a function of the thickness of the carbonate layer. The frequency is 300 Hz.

3.2 Synthetic seismograms and migration analysis

The calculation of synthetic seismograms can be used to establish proper seismic experiments to locate the septaria, test inversion algorithms, and analyse the proper frequency bandwidth to differentiate between single geobodies; in summary, the modelling is essential to locate the septaria. The seismograms are computed with a modelling code based on the anisotropic and viscoelastic stress–strain relation introduced above. The time–space differential equations were first introduced by Carcione (1990). The algorithm is based on the Fourier pseudospectral method for computing the spatial derivatives and a fourth-order Runge–Kutta technique for calculating the wavefield recursively in time (Carcione *et al.* 2012; Carcione 2015).

First, we compute snapshots of the wavefield in the Boom Clay to analyse the radiation pattern of different sources. To compute the transient responses, we use a Ricker wavelet of the form given in Appendix G. Fig. 19 shows snapshots corresponding to the elastic (a) and viscoelastic (b) cases for an explosive source ($f_{xx} = f_{zz}$), with a dominant frequency of 300 Hz (compare with Fig. 11a). The snapshot in (b) has been enhanced 10 times with respect to the lossless case (a). Loss of high frequencies and attenuation can be observed in (b). The snapshot for a pure shear source (f_{xz} only differs from zero) is shown in Fig. 20. In this case, the shear wave is dominant. In both cases, pure dilatational and pure shear sources, the coupling due to anisotropy is significant, that is, contrary to the isotropic case, where each source generates energy of its own characteristics.

We perform several seismic numerical experiments for the analysis and interpretation of the experimental data. We consider four different geological models with increasing complexity. From the anisotropy parameters obtained from the inversion of the shots given in Table 1, we compute the parameters of the Boom Clay given in Table 2. This medium constitutes the background material for the numerical simulations. The anisotropy parameters ϵ and δ are the average of the five shots given in Table 1. Isolated and/or distributed septaria forming layers are also considered. Since the equation of motion is linear, seismograms with different time histories and frequency bandwidth can be implemented by convolving $w(t)$ with only one simulation using $\delta(t)$ as a source – a discrete delta with strength $1/\mathrm{d}t$.

The geological models are discretized on a numerical mesh. All simulations use 1001 × 715 grid points with a spacing of 12.5 cm. The offset is referred to the well-head position (see also Fig. 3b). Absorbing boundary conditions are implemented at the bottom and lateral edges of the model, with absorbing strips, to avoid wraparound effects, typical of pseudospectral algorithms. The horizontal absorbing strips are 110 point wide, while the vertical ones have 150 points, corresponding to 13.75 and 18.75 m, respectively. The source time history is the Ricker wavelet indicated above. The dominant frequency is 960 Hz. Unless differently indicated, the source is an explosion.

We perform two different modelling experiments: (i) RVSP simulations with the same geometry of shot 52 (source depth at 48 m); (ii) plane-wave simulations with sources located at 1.5 m depth, to mimic the geometry of the seismic survey performed in 2013 at the Kruibeke test site (Eddie 2014). Instead of using point sources to compute shot gathers to be processed with the standard sequence, we perform simulations that approximate unmigrated zero-offset sections by triggering simultaneously sources located at each grid point in the upper edge of the numerical mesh (Carcione *et al.* 1994). This procedure generates a plane wave propagating downwards. The plane wave is then reflected back to the surface when it hits an interface separating two different formations (i.e. the

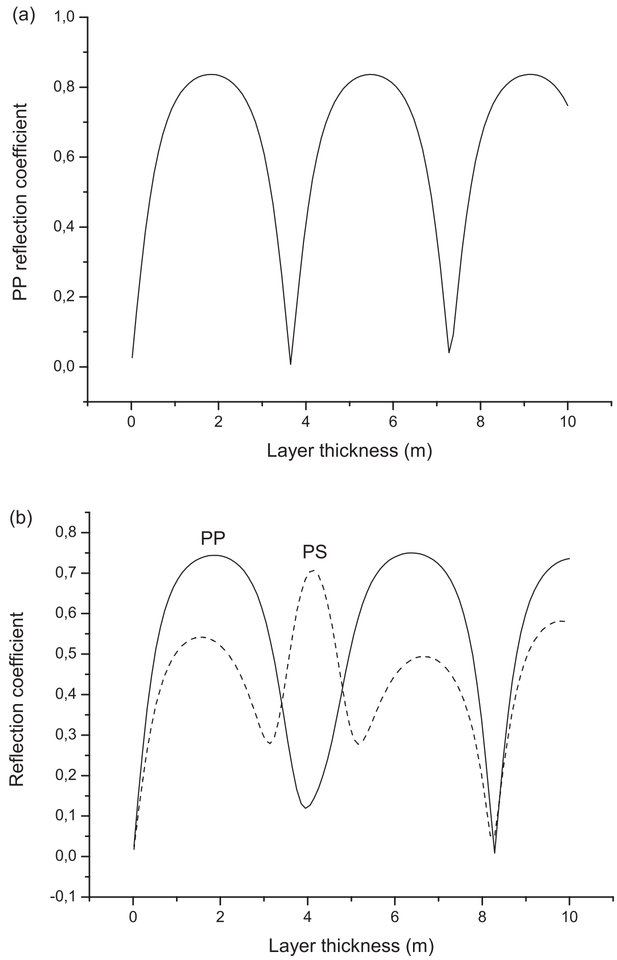

Figure 17. Reflection coefficients at normal incidence (a) and at 20° (b) as a function of the thickness of the carbonate layer. The frequency is 600 Hz.

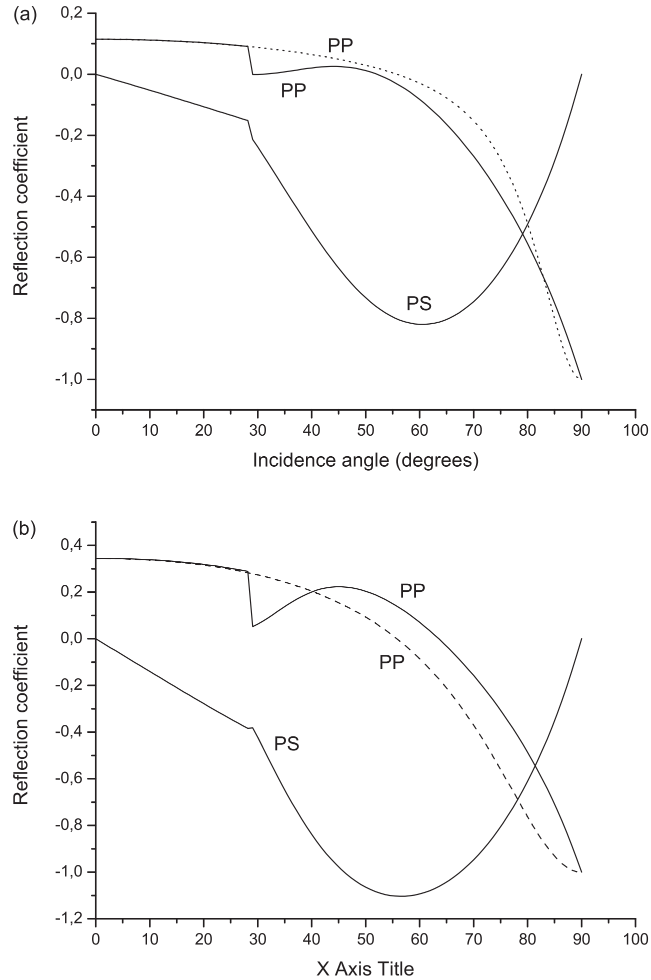

Figure 18. Reflection coefficients as a function of the incidence angle, where the solid lines corresponds to the exact expression, while the dashed line to an approximation that neglects the *S* wave. Plots (a) and (b) refer to $h = 0.5$ m and $h = 1$ m, respectively. The frequency is 300 Hz.

septaria layers in this study). Eventually, the seismic wave is recorded by sensors located close to the Earth surface, in agreement with the coordinates of the sensors in the field. This technique dramatically reduces the computer time to obtain an interpretable seismic section. Each modelling experiment is computed in the elastic and viscoelastic cases, that is, with the quality factors of the clay equal to infinity or with the values given in Table 2.

3.2.1 *Single septarium*

The model is given in Fig. 21, where a calcium carbonate object is embedded in the Boom Clay. The orange areas at the lateral edges and at the bottom of the model are absorbing strips. With this simple scheme, we perform the imaging of a single septarium, which has dimensions 1 m × 1 m. As mentioned above, we have performed two modelling experiments, a single shot simulation reproducing the geometry of shot 52 and a plane-wave simulation. Moreover, both the elastic (no attenuation) and viscoelastic seismograms are computed. The red star in Fig. 21 shows the source location for the single-shot simulation.

Fig. 22 shows the plane-wave simulations in the elastic (a) and anelastic (b) cases, that is, without and with attenuation. Both seismograms have the diffraction events caused by the septarium, but panel (b) is characterized by lower frequencies due to attenuation. Panels (c) and (d) represent the seismic sections given in panels (a) and (b) after time migration. The diffraction events are collapsed revealing the correct position of the septarium in time. To migrate the seismic data, we have used a time–wavenumber domain algorithm implemented in the Seismic Unix software package (Stockwell & Cohen 2008).

The different panels in Fig. 22 are represented with different scaling values in order to clearly visualize the seismic signal. This means that the amplitude of the waves indicated by the intensity of the colours (black or white) is not directly comparable between adjacent panels. Due to the attenuation, the amplitudes in the seismograms of panels (b) and (d) are two orders of magnitude lower than the amplitudes of the seismograms of panels (a) and (c), respectively. This aspect becomes clear in Fig. 23, where the left part of the diffraction event comes from Fig. 22(b), while the right part from Fig. 22(a). We show simulations with two set of attenuation coefficients, where case (b) is an upper limit. In these plots, the same scaling is applied to the viscoelastic and elastic seismograms and the amplitude loss due to attenuation is quite evident. The apparent polarity inversion between the left and right parts of Fig. 23 is the effect of the variation of the shape of the seismic pulse due to velocity dispersion caused by attenuation. The high- frequency components of the seismic signal are attenuated more rapidly than the low-frequency components, causing the variation of the shape of

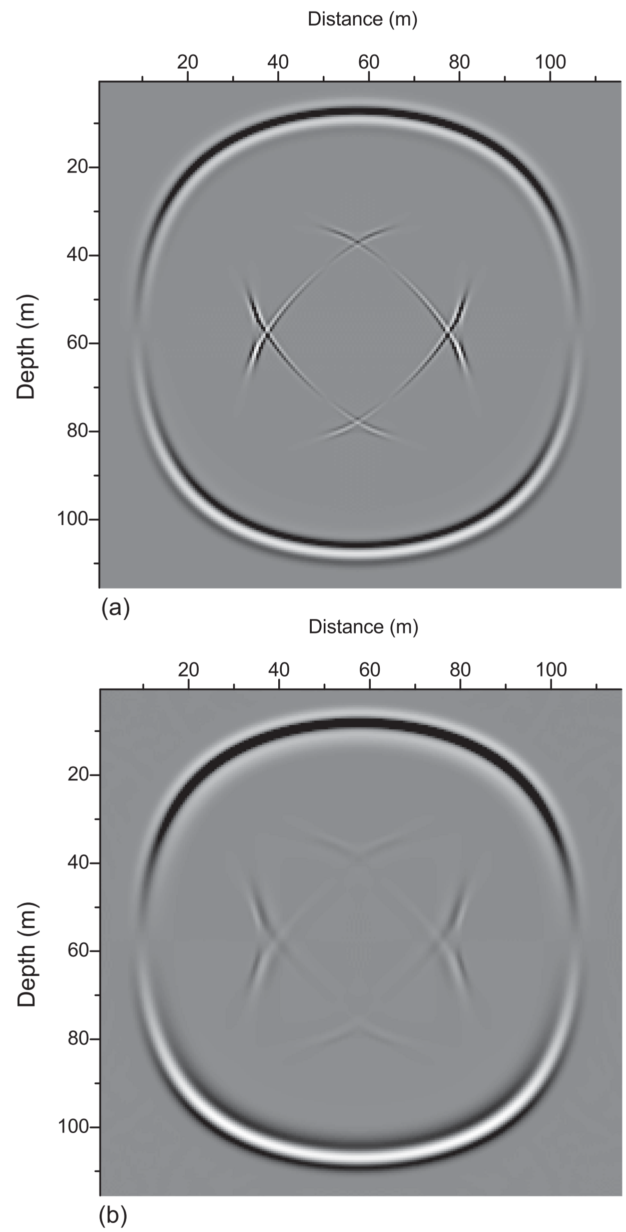

Figure 19. Snapshots of the vertical component of the particle velocity for a propagation time of 35 ms, (a) lossless case, (b) lossy case. The source is dilatational and its dominant frequency is 300 Hz. The snapshot in (b) has been enhanced 10 times with respect to the lossless snapshot (a).

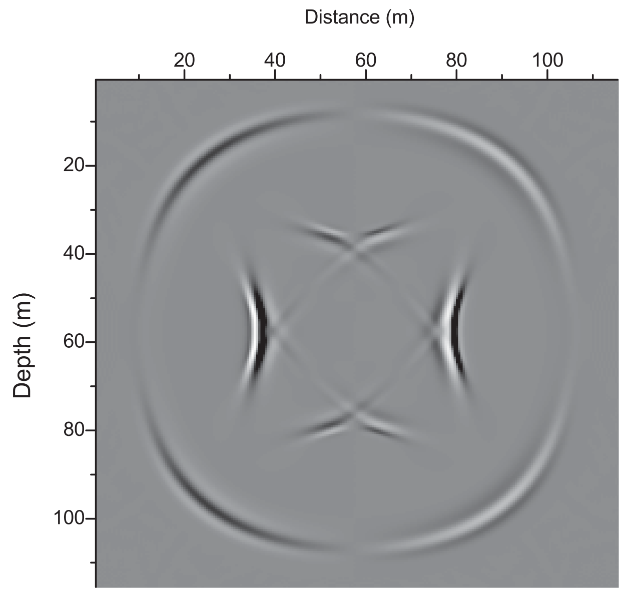

Figure 20. Snapshot of the vertical component of the particle velocity for a propagation time of 35 ms. The source is pure shear motion and its dominant frequency is 300 Hz and the medium is lossy.

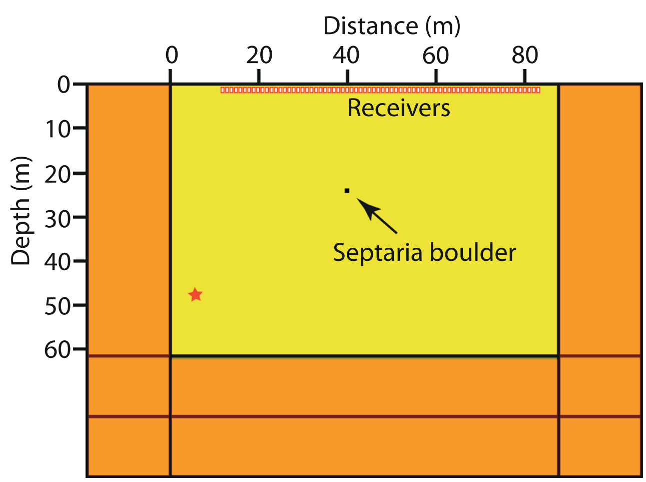

Figure 21. Model used for the first RVSP simulation, with a single septarium. The source is indicated by a red star. The orange areas correspond to absorbing strips.

the pulse. A different gain for the elastic and viscoelastic synthetic data is applied hereafter.

Fig. 24 shows a single-shot simulation in the elastic and viscoelastic cases, respectively. The diffraction event generated by the septarium is clearly identifiable on both seismograms, although seismic signals in panel (b) are characterized by lower frequencies compared to the elastic case. The red line is the first break pick. Panels (c) and (d) show the shot simulation for an isotropic background in the elastic and anelastic cases, respectively. We consider the same properties of Table 2 but the anisotropy parameter ϵ and δ of the Boom Clay are set to zero. The red line in panels (a) and (b) represent the picking of the first break and the same lines are plotted in panels (c) and (d), respectively, with the purpose of underlining the importance of considering anisotropy in seismic interpretation.

On the other hand, Fig. 25 shows the seismograms due to a vertical force, which generates *P* and *S* waves. In this case, the different events can be observed and it is clear that proper simulations should consider attenuation and anisotropy but also the complete stress–strain relation bases on dilatational and shear deformations, otherwise the amplitudes and phase are not realistic. In Fig. 25, *P* and *S* are the direct *P*- and *S*-waves generated by the source, PPd is the diffraction event and PSd are *S*-waves caused by the wave front *P* hitting the septarium, while SPd and SSd are the diffraction events and *S* waves caused by the *S* wave front hitting the septarium.

The relationship between the width of the septarium and its seismic image width is defined by the Fresnel zone, which is a measure of the horizontal resolution. Geobodies smaller than the Fresnel zone usually cannot be detected using seismic waves, but seismic migration may highly improve the resolution. Since the vertical

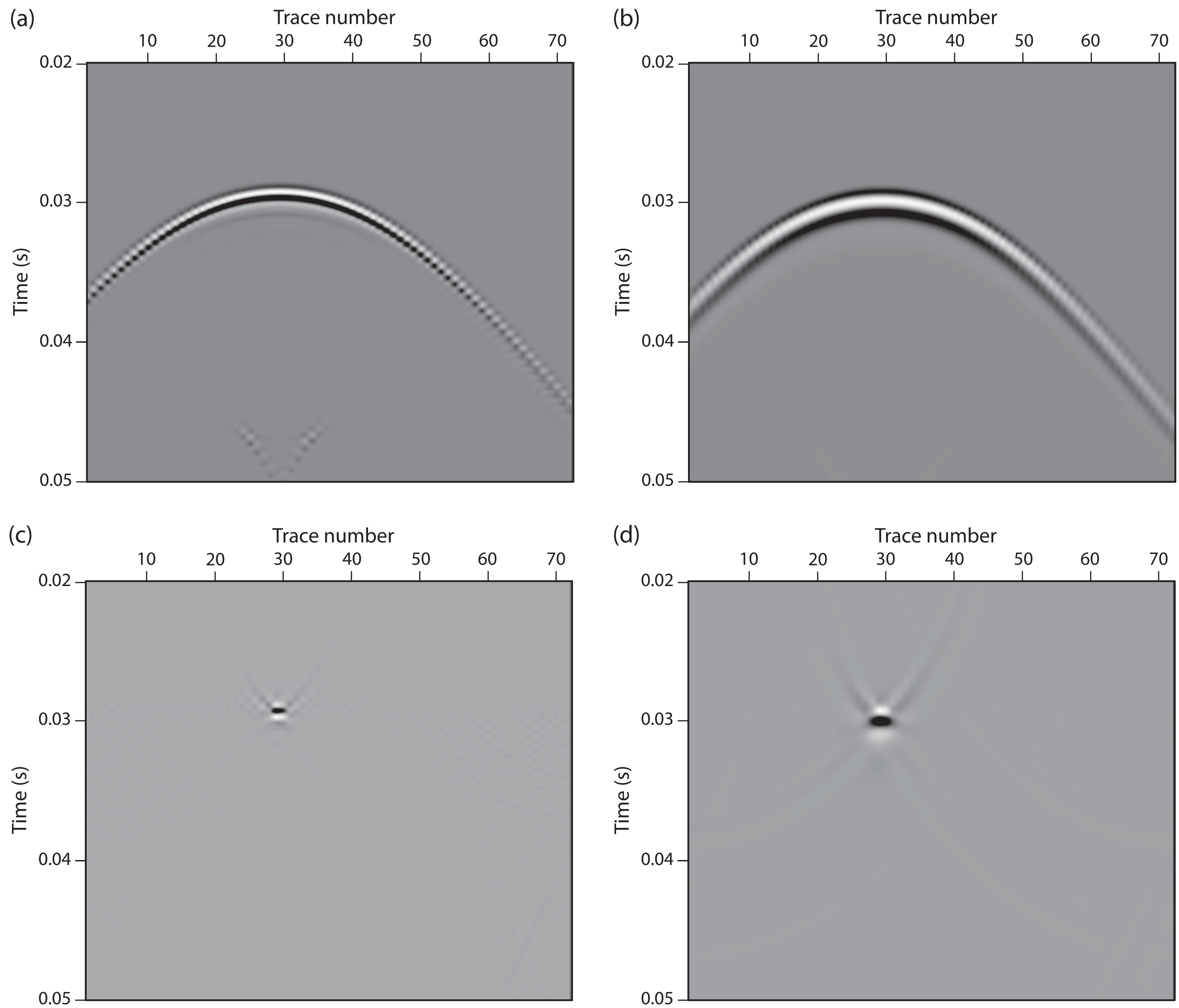

Figure 22. Seismograms from the plane-wave simulations for the elastic (a) and viscoelastic (b) cases before migration and after migration (c) and (d), respectively.

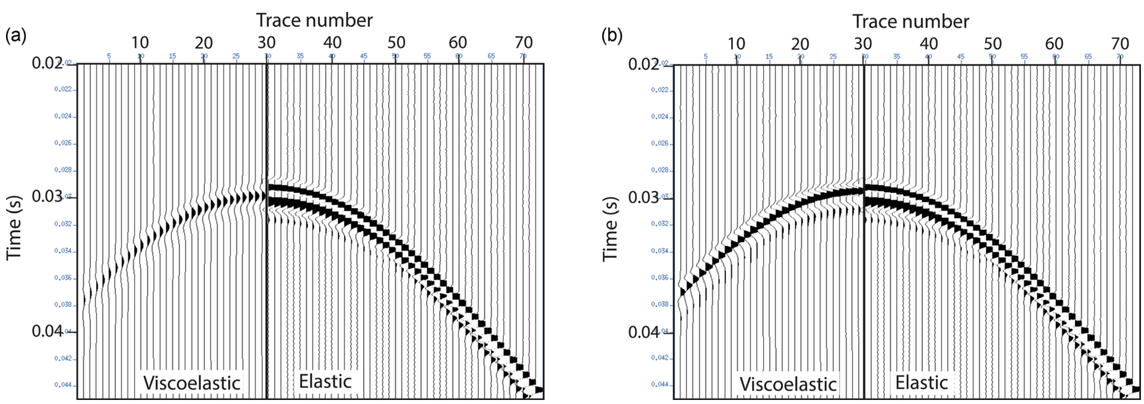

Figure 23. Seismograms showing a qP-wave reflection event in the viscoelastic (left) and elastic (right) cases: (a) $Q_P = 20$ and $Q_S = 10$; (b) $Q_P = 40$ and $Q_S = 30$.

resolution is $\lambda/4$, where λ is the wavelength, the horizontal resolution before migration, represented by the Fresnel radius, is

$$R = \sqrt{\left(z^2 + \frac{\lambda}{4}\right)^2 - z^2} \approx \sqrt{\frac{\lambda z}{2}}, \tag{6}$$

where z is the reflector depth (Elmore & Heald 1969). Migration is a downward continuation of the seismic energy from the receivers to the reflectors such that the theoretical limit is obtained for $z = 0$, that is, after migration the Fresnel radius is $R = \lambda/4$. For a frequency of 300 Hz and a velocity of 1637 m s^{-1}, the Fresnel radius before

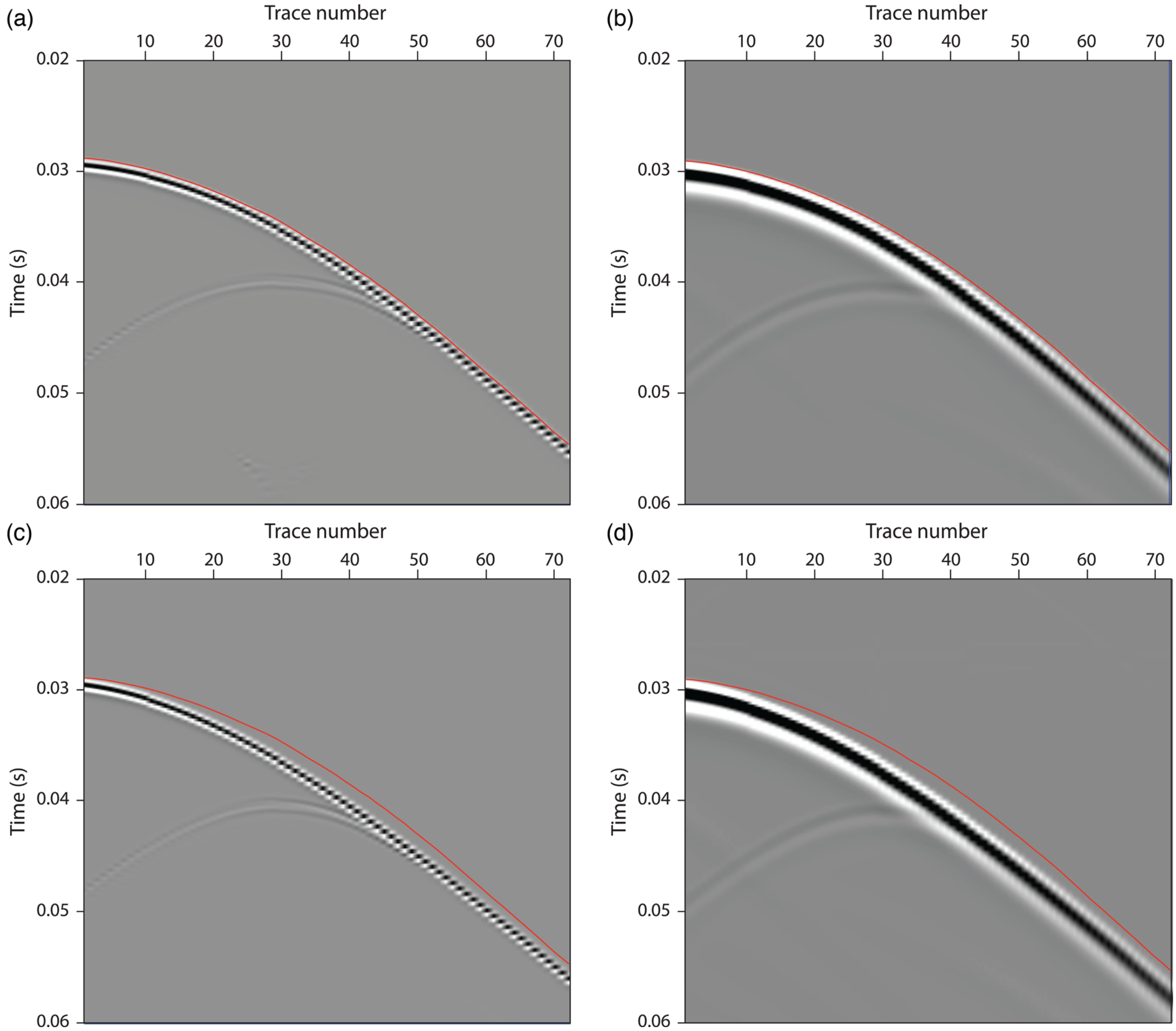

Figure 24. Seismograms due to a single shot corresponding to the anisotropic elastic (a), anisotropic viscoelastic (b), isotropic elastic (c), isotropic viscoelastic (d) cases. The source is an explosion.

and after migration are $R \approx 1.65\sqrt{z}$ and $R = 2.7$ m, respectively. At $z = 70$ m, for instance, before migration the Fresnel radius is 14 m, so the resolution highly improves. A relevant reference for a numerical investigation of the detectability and resolvability of inclusions is Zhan *et al.* (2014).

3.2.2 *Multiple septaria*

In this test, we explore the capability of the seismic method to identify isolated septaria having different shapes and sizes. We consider six isolated septarias embedded in the clay material. Properties of the media are reported in Table 2. Fig. 26 shows the geological model with the septaria in black and located at 15 m depth. Let us number these objects 1 to 6 from left to right; their dimensions are given in Table 3. Figs 27(a) and (b) show the unmigrated plane-wave elastic and anelastic seismic sections, respectively. Each diffraction event in both pictures corresponds to a septarium. The seismic signal in panel (b) is characterized by a lower frequency content compared to panel (a) because of attenuation.

The time-migrated sections of the synthetic data in panels (a) and (b) are shown in panels (c) and (d), respectively. The diffraction events have correctly collapsed to their apex. The dimensions of the septaria boulders can qualitatively be estimated from the migrated seismic sections as the reflections length and strength increase proportionally to the size of the boulders. Fig. 28 shows a seismic gather corresponding to shot 52 in the elastic (a) and anelastic (b) cases. Each septarium generates a diffraction event on the seismic section.

3.2.3 *Multiple septaria layers*

The model considered for this simulation is given in Fig. 29. Here, we study the seismic response of discontinuous layers of septaria. We model ten septaria horizons equally spaced in depth. The first layer is located at 10 m depth and the vertical distance between two adjacent layers is 3.5 m. The thickness of the septaria layers is 0.5 m and within each layer the relative quantity of the calcareous material with respect to clay increases with depth, whose percentage in each layer is given in Table 4. Moreover, the septaria are randomly distributed within each layer. We computed plane-wave and single-shot synthetic data. Panels (a) and (b) of Fig. 30 show the elastic and viscoelastic plane-wave simulations, while panels (c) and (d) display the corresponding migrated seismic sections. Panels (b) and

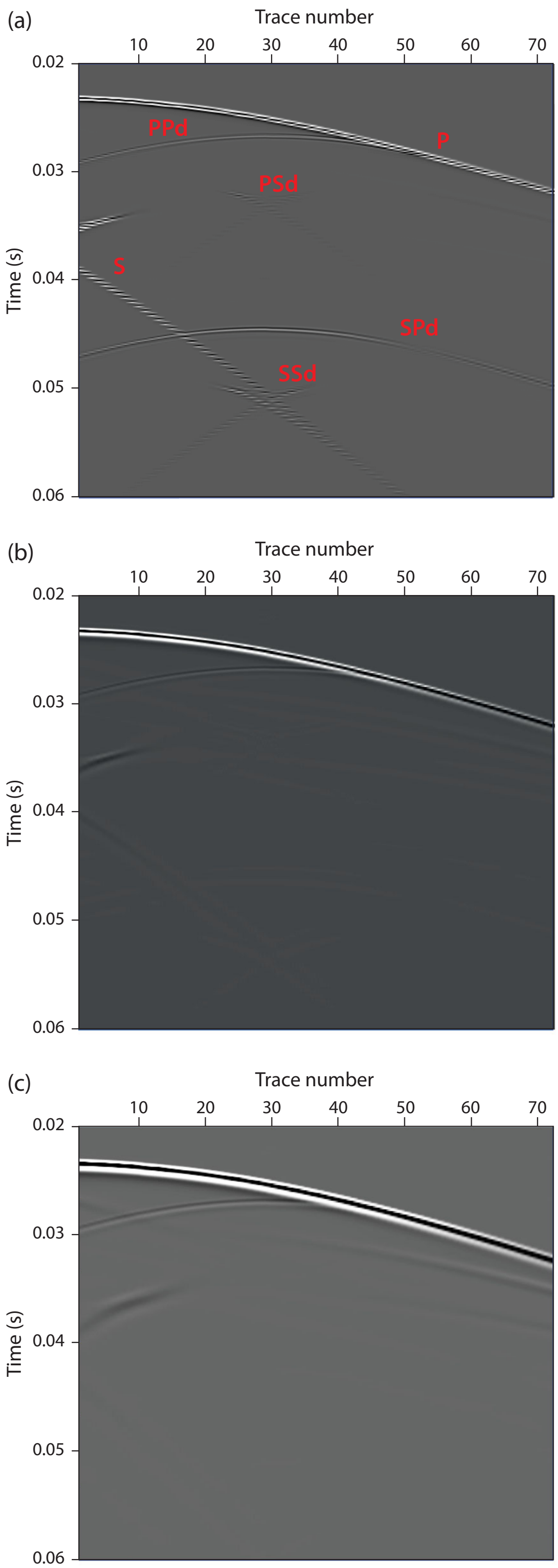

Figure 25. Seismograms due to a single shot corresponding to the anisotropic elastic (a) and anisotropic viscoelastic cases: (b) $Q_P = 20$ and $Q_S = 10$; (c) $Q_P = 40$ and $Q_S = 30$. The source is a vertical force.

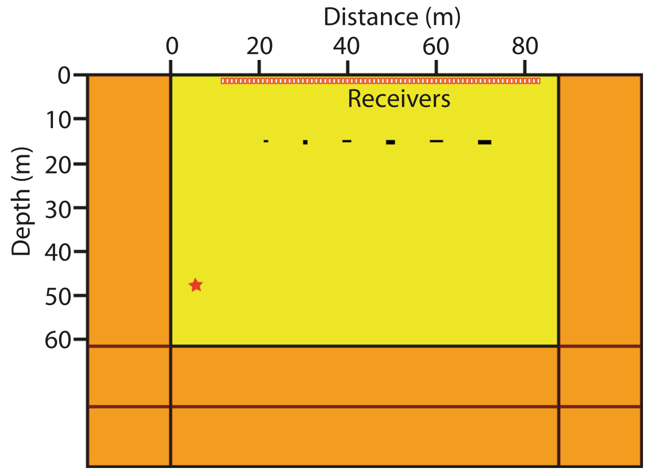

Figure 26. Model used for the RVSP experiment with multiple septaria of different sizes.

Table 3. Size of septaria objects.

Septaria #	Width (cm)	Thickness (cm)
1	100	50
2	100	100
3	200	50
4	200	100
5	300	50
6	300	100

(d) are characterized by lower frequencies compared to the elastic seismic sections. This is a typical effect of seismic attenuation.

Two important aspects become evident from the analysis of these images. The first is related to the quantity of carbonate in the different septaria layers. Even a very small quantity of calcareous material generates a seismic horizon relatively continuous, especially in the unmigrated sections. However, Figs 30(a) and (b) show diffraction events in the first three seismic horizons at 0.013, 0.018 and 0.022 s, approximately, where the percentage of carbonate in the layers are 5, 10 and 15 per cent (see also Table 4). The discontinuity of the septaria layer decreases as the carbonate content increases and the seismic image of the layer tend to be a continuous reflection. The second aspect is related to the number of reflections identifiable in the seismic sections. Despite the presence of ten septaria layers in the geological model (Fig. 29), 13 seismic horizons can be identified in panel (b) of Fig. 30. This is due to multiple reflections caused by the layering. An erroneous interpretation of the seismic horizons could lead to an overestimation of the number of septaria layers present in the formation. The interpretation of seismic sections from field data should be supported by well-log data and synthetic data to avoid a possible overestimation of the septaria layers.

Fig. 31 shows the results of the single-shot simulation in the elastic (a) and anelastic (b) cases. The events at approximately one-way traveltimes of 0.035, 0.04 and 0.045 s are seismic signals caused by the layering. Diffraction events related to possible isolated septaria boulders can hardly be identified in these two seismograms.

3.2.4 *Simulation of the real stacked seismic data*

Fig. 32 shows the stacked section obtained from the field data. We applied a specific seismic processing sequence to enhance the continuity of the seismic horizons, in particular we applied a bandpass

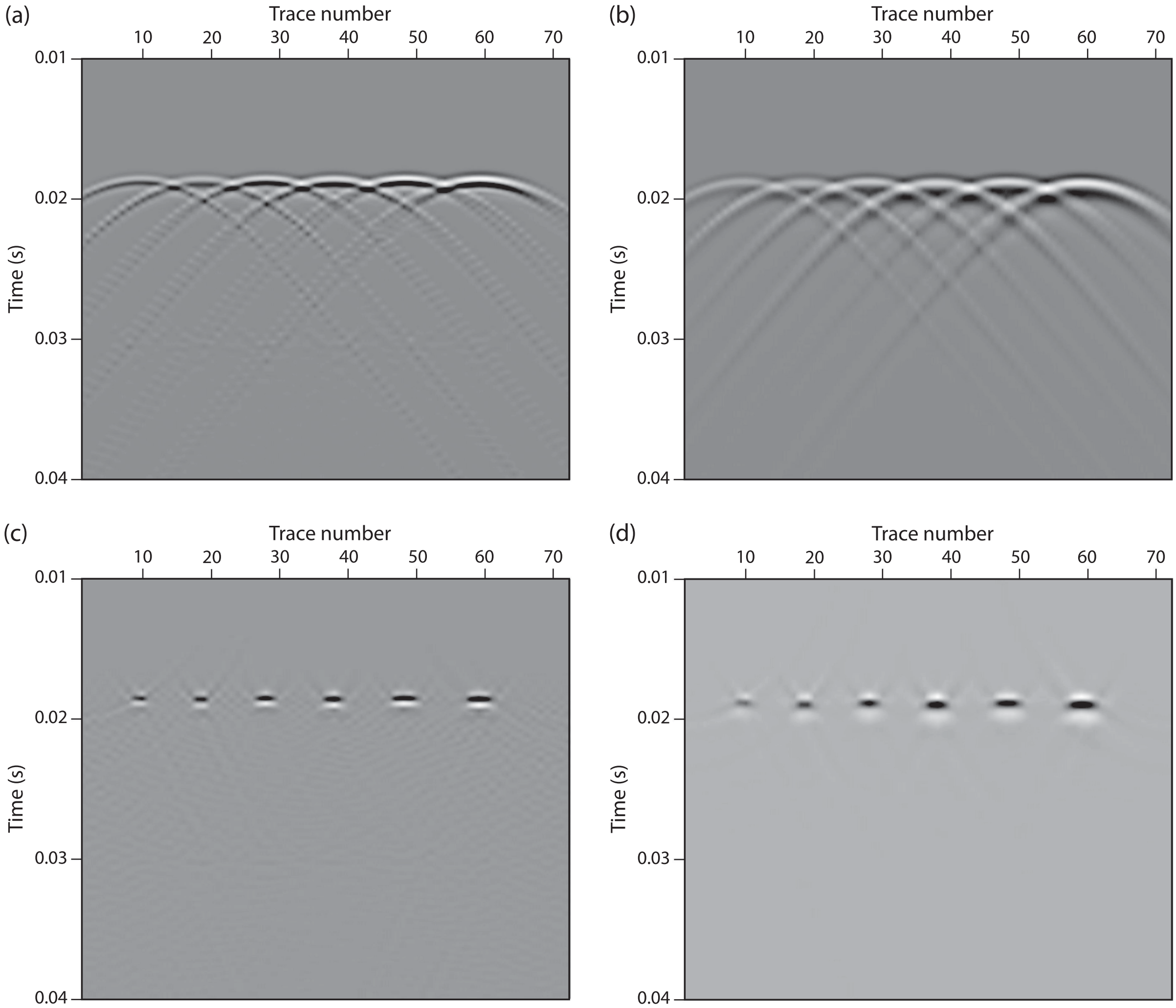

Figure 27. Stacked seismograms corresponding to the model of Fig. 26.

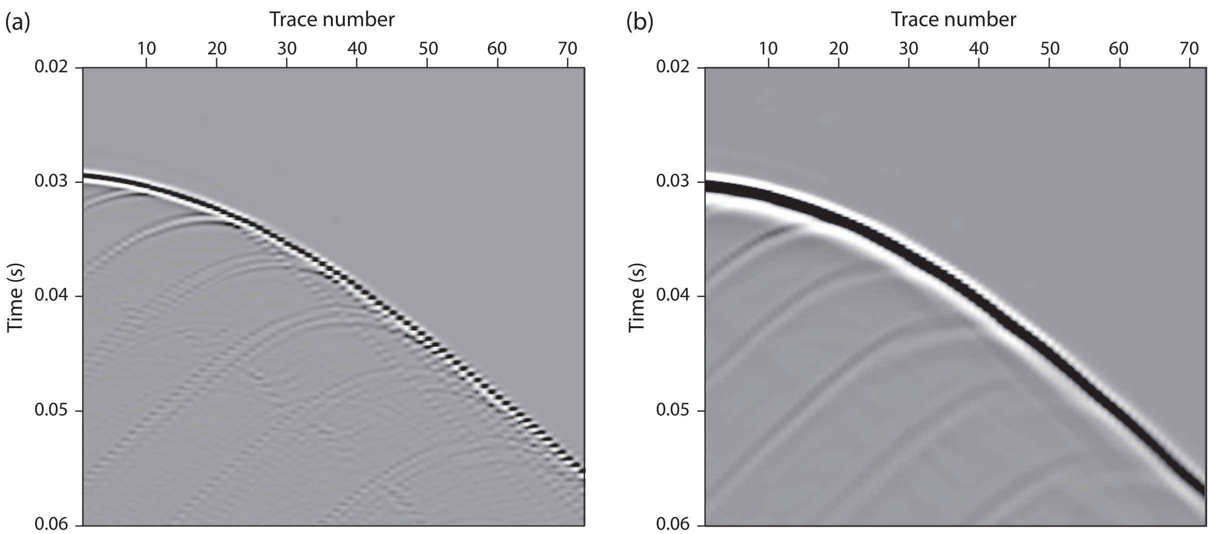

Figure 28. Seismic gather corresponding to shot 52 in the elastic (a) and anelastic (b) cases.

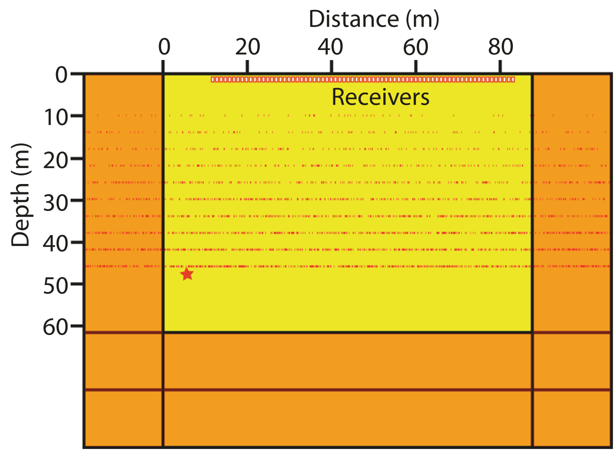

Figure 29. Geological model used to simulate a stacked section.

Table 4. Percentage of calcareous material in each septaria layer.

Layer #	Depth (m)	Per cent of carbonate
1	10	5
2	14	10
3	18	15
4	22	20
5	26	25
6	30	30
7	34	35
8	38	40
9	42	45
10	46	50

filter with corner frequencies 80–120 and 800–1000 Hz to damp high-frequencies. The red lines are a line-drawing indicating strong reflections, which are not necessarily related to septaria layers but possibly to intra-bed multiples as pointed out above.

Fig. 33 shows the geological model. The Boom Clay is indicated by the yellow colour and the carbonate concretions by the red thin layers. The seismic properties of these two litho-types are given in Table 2. The septaria layers are specifically designed to reproduce, in the plane-wave synthetic seismic section, the reflections indicated by the line-drawing in Fig. 32. As those events may be related to multiple reflections, the geological model does not necessarily correspond to the real stratigraphy in the field.

Figs 34(a) and (b) show the unmigrated plane-wave seismic sections for the elastic and viscoelastic cases, respectively. Primary

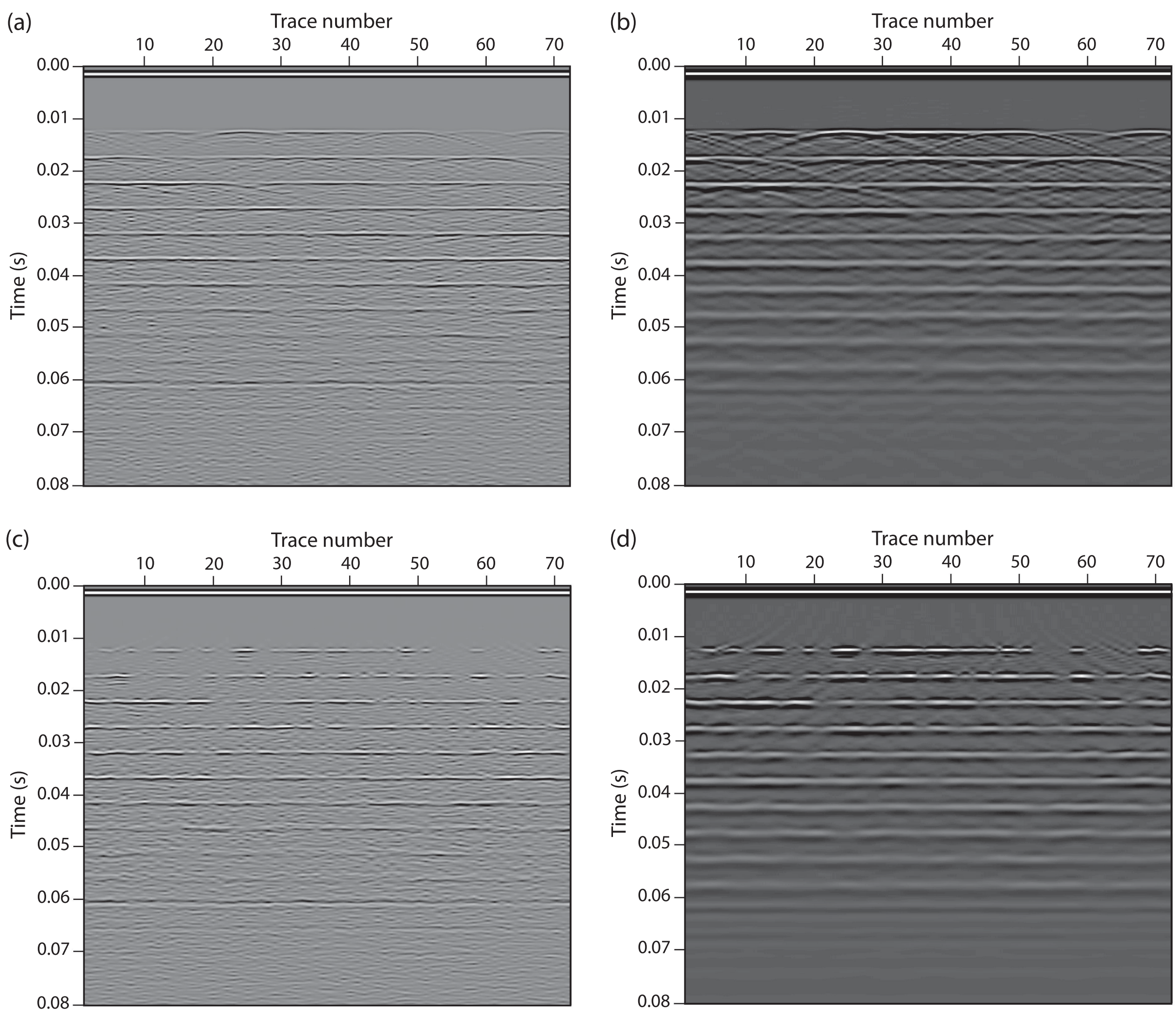

Figure 30. Stacked seismograms for the elastic (a) and viscoelastic (b) cases and their corresponding migration results (c) and (d), respectively.

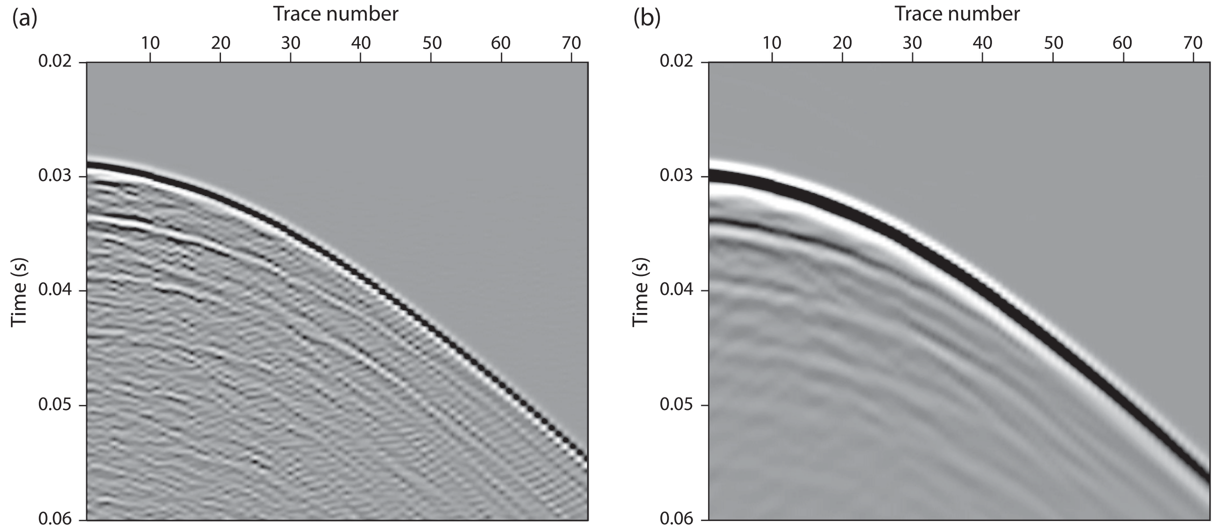

Figure 31. Single-shot seismograms corresponding to the anisotropic elastic (a) and anisotropic viscoelastic (b) cases.

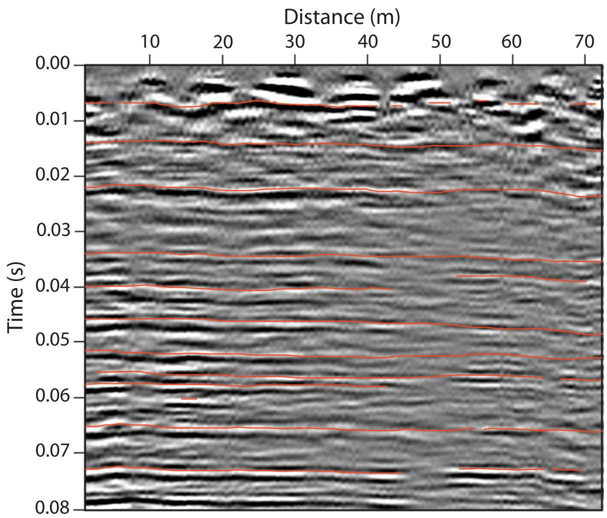

Figure 32. Stacked seismic section from field data.

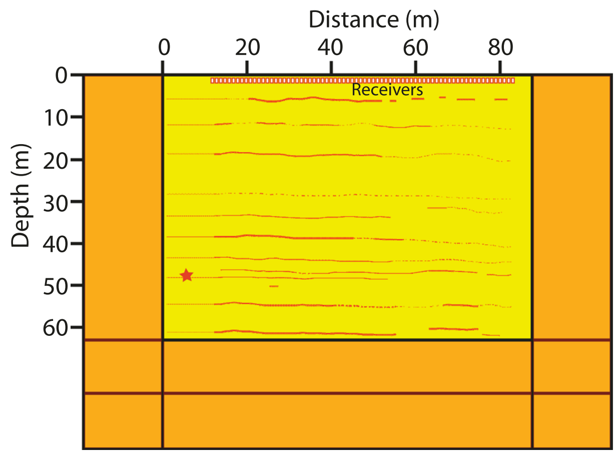

Figure 33. Geological model used to simulate the stacked section of Fig. 32.

reflections are indicated by the line-drawing. Other signals in the synthetic seismic section are intra-bed multiple reflections caused by the layering. We have considered a Ricker wavelet source time-history with a peak frequency of 500 Hz. Panels (c) and (d) show the migration of the synthetic data of panels (a) and (b), respectively. Migration correctly reconstructs the time position of the seismic horizons and provides an estimation of the continuity (or discontinuity) of the layer. Moreover, the thickness of the septaria layers can be evaluated from the amplitude of the reflection events.

Figs 35(a) and (b) are single-shot seismograms without and with attenuation, respectively. Events due to the layering can easily be identified, for example, at approximately 0.038, 0.048, 0.052 s, while diffraction events due to possible isolated calcareous boulders can hardly be recognized in the sections.

4 CONCLUSIONS

We have characterized the seismic properties of the Boom clay based on seismic experiments at the Kruibeke site and computed synthetic seismograms with embedded distribution of septaria. We have used the most reliable information available, that is, laboratory data and VSP traveltimes from field experiments. The inversion allowed us to obtain the *P*-wave properties of the Boom Clay, including the anisotropy parameters. These results were constrained by further information published in the literature as seismic, log and laboratory data. In particular, the *S*-wave related properties were obtained by taking into account the physical realizability of the Boom Clay. Attenuation has been estimated from a similar clay (having similar seismic velocities), in particular, Pierre Shale from Limon, Colorado, USA.

We have performed *P*-wave arrival-time inversions of the five deepest RVSP shots. This inversion gives the Thomsen anisotropy parameters ϵ and δ of an equivalent homogeneous medium. The inversions give quite consistent results although the symmetry of the medium is unusual as the inverted ϵ is negative. To prove the effectiveness of the methodology we have performed numerical simulations with the inverted seismic properties and matched the picked arrival time for the deeper shot of the RVSP field experiment. The negative sign of ϵ is an aspect which needs to be clarified and we suggest new data acquisition, both RVSP and reflection seismic with two lines of surface receivers perpendicular to each other. This geometry of acquisition allows the detection of azimuthal anisotropy. The stress–strain relation describes anisotropy and

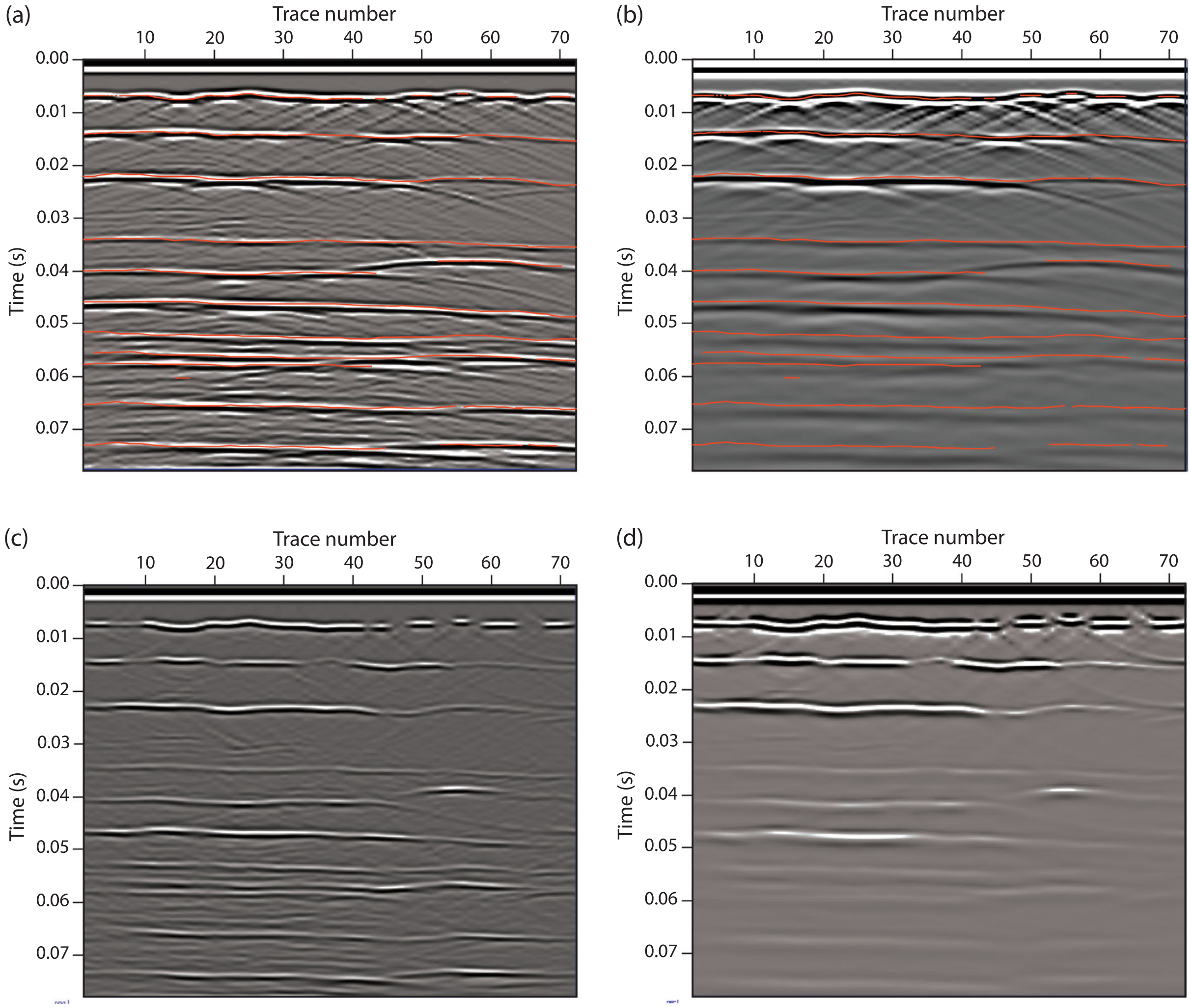

Figure 34. Stacked seismograms for the elastic (a) and viscoelastic (b) cases and their corresponding migration results (c) and (d), respectively.

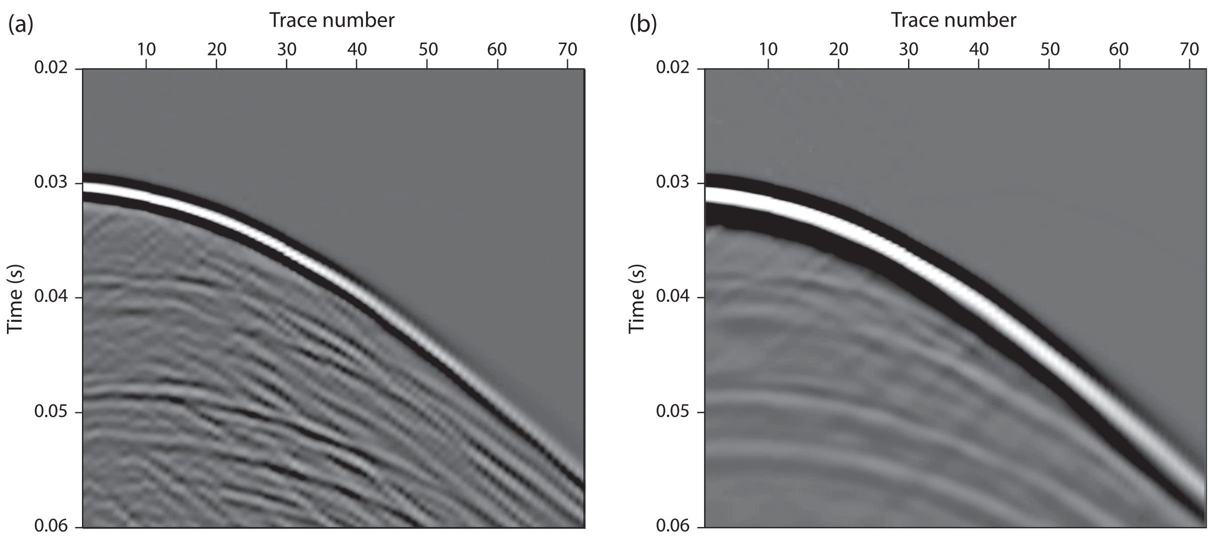

Figure 35. Single-shot seismograms corresponding to the anisotropic elastic (a) and anisotropic viscoelastic (b) cases.

attenuation based on the Zener model, since a velocity-dispersion analysis based on several frequency bands up to 900 Hz indicates that the wave velocity increases with frequency.

We have computed reflection coefficients of septaria bodies at 300 Hz. At normal incidence the coefficient vanishes at specific thicknesses of the septarium and there is no conversion to the *S* wave. At 20°, the conversion is remarkable and maximum PP coefficients occur for thicknesses between 3 and 5 m. Similar plots for 600 Hz show that for thicknesses of 1 m the septarium can be detected more easily since the amplitudes are higher (nearly 0.8). Converted PS energy offers an additional possibility to detect the carbonate layers, since the *S*-wave energy shows a maximum where the *P*-wave energy is weak, for instance at 4 m thickness. It is recommended to perform AVO studies on both PP and PS events to avoid ambiguities in the interpretation. More information can be obtained by computing the reflection coefficients as a function of the incidence angle. It is shown that the acoustic rheology (only *P* waves) is an acceptable approximation. A transition angle at nearly 30° implies a notable variation at large offsets. Converted PS waves have a high amplitude at large offsets (between 30° and 80°) and can be useful to identify the target on this basis.

Moreover, we have investigated the effect of septaria embedded in the Boom Clay with several numerical simulations, for horizontal partial and complete continuity of the calcareous inclusions. Particularly, we have considered four different models: a single isolated septarium, six septaria bodies differing in size, discontinuous layers of inclusions with increasing frequency of the carbonate material, and septaria layers to give a plane-wave section similar to the stacked section from the available experimental data set. The simulations with layers of calcareous material show continuity of the reflections even when the percentage of carbonate within the layer with respect to the clay is very small (5–15 per cent). This is particularly evident in the unmigrated seismic sections. However, for low content of the calcareous material, isolated septaria boulders generate diffraction events, which are hardly distinguishable for high carbonate content in the layer and the seismic horizons appear quite continuous. The synthetic experiment predicts the main reflections of the stacked seismic section obtained from the field data reasonably well regardless that the geological model does not necessarily correspond to the field stratigraphy. Numerical simulations with multilayered septaria layers generate seismic images with intra-bed multiple reflections due to the layering. The interpretation of seismic sections from field data should be supported by well-log data and synthetic seismic data to avoid overestimations of the number of septaria layers.

Further research involves a Fresnel-zone analysis to quantify the percentage of carbonate, modelling of the Boom Clay with fine layers to obtain a negative anisotropy parameter ϵ, the description of the Boom Clay with a poroelasticity stress–strain relation and the use of *Q* compensation techniques to enhance the images of the septaria.

ACKNOWLEDGEMENTS

This work was funded by ONDRAF-NIRAS (Belgian Agency for Radioactive Waste and Enriched Fissile Materials). We thank Prof Antonio Gonzalez-Fernandez for useful comments.

REFERENCES

Abels, H.A., Simaeys, S.V., Hilgen, F.J., De Man, E. & Vanderberghe, N., 2007. Obliquity-dominated glacio-eustatic sea level change in the early Oligocene: evidence from the shallow marine siliciclastic Rupelian stratotype (Boom Formation, Belgium), *Terra Nova,* **19,** 65–73.

Alkhalifah, T. & Tsvankin, I., 1995. Velocity analysis for transversely isotropic media, *Geophysics,* **60,** 1550–1566.

Auld, B.A., 1990. *Acoustic Fields and Waves in Solids,* vol. II, 2nd edn, R. E. Krieger.

Backus, G.E., 1962. Long-wave elastic anisotropy produced by horizontal layering, *J. geophys. Res.,* **67,** 4427–4440.

Berryman, J.G., Grechka, V.Y. & Berge, P.A., 1999. Analysis of Thomsen parameters for finely layered VTI media, *Geophys. Prospect.,* **47**(6), 959–978.

Carcione, J.M., 1990. Wave propagation in anisotropic linear viscoelastic media: theory and simulated wavefields, *Geophys. J. Int.,* **101,** 739–750. Erratum: 1992, 111, 191.

Carcione, J.M., 1999. Staggered mesh for the anisotropic and viscoelastic wave equation, *Geophysics,* **64,** 1863–1866.

Carcione, J.M., 2015. *Wave Fields in Real Media. Theory and Numerical Simulation of Wave Propagation in Anisotropic, Anelastic, Porous and Electromagnetic Media,* 3rd edn, revised and extended, Elsevier Science.

Carcione, J.M., Böhm, G. & Marchetti, A., 1994. Simulation of a CMP seismic section, *J. Seism. Explor.,* **3,** 381–396.

Carcione, J.M., Quiroga-Goode, G. & Cavallini, F., 1996. Wavefronts in dissipative anisotropic media: comparison of the plane wave theory with numerical modeling, *Geophysics,* **61,** 857–861.

Carcione, J.M., Poletto, F. & Farina, B., 2008. Simulation of axis-symmetric seismic waves in fluid-filled boreholes in the presence of a drill string, *Comput. Geosci.,* **12,** 593–604.

Carcione, J.M., Gei, D., Picotti, S. & Michelini, A., 2012. Cross-hole electromagnetic and seismic modeling for CO_2 detection and monitoring in a saline aquifer, *J. Pet. Sci. Eng.,* **100,** 162–172.

De Craen, M., Wang, L., Van Geet, M. & Moors, H., 2004. Geochemistry of Boom Clay pore water at the Mol site Status 2004, Scientific Report SCKCEN-BLG-990, 04/MDC/P-48

Eddies, R., 2014. Ondraf/Niras Kruibeke test site seismic investigation, Fugro report.

Elmore, C.W. & Heald, A.M., 1969. *Physics of Waves,* McGraw-Hill.

Gei, D., 2013. Investigation and derivation of anisotropic parameters from microseismic reservoir monitoring, *PhD thesis,* University of Trieste.

Gei, D., Eisner, L. & Suhadolc, P., 2011. Feasibility of estimating vertical transverse isotropy from microseismic data recorded by surface monitoring arrays, *Geophysics,* **76**(6), WC117–WC126.

Grechka, V. & Tsvankin, I., 1998. Feasibility of nonhyperbolic moveout inversion in transversely isotropic media, *Geophysics,* **63,** 957–969.

Hemerijckx, E., Carpentier, R., De Schrijver, P., Henriet, J.P. & Heldens, Ph., 1983. Preliminary investigation of concretion horizons in a Tertiary clay layer in view of the construction of a pre-metro tunnel under the river Scheldt at Antwerp (Belgium), in *Proceedings of the International Symposium on Engineering Geology and Underground Construction,* Lisbon, 1.53–1.70.

Lynn, W., Gonzalez, A. & MacKay, S., 1991. Where are the fault- plane reflections?, in *61st Annual International Meeting,* SEG, Expanded Abstracts, pp. 1151–1154.

Marelli, S., Manukyan, E., Maurer, H., Greenhalgh, S.A. & Green, A.G., 2010. Appraisal of waveform repeatability and reliability for crosshole and hole-to-tunnel seismic monitoring of radioactive waste repositories, *Geophysics,* **75,** Q21–Q34.

Marutyan, K.R., Holland, M.R. & Miller, J.G., 2006. Anomalous negative dispersion in bone can result from the interference of fast and slow waves, *J. acoust. Soc. Am.* **120**(5), EL55–EL61.

Mavko, G., Mukerji, T. & Dvorkin, J., 2009. *The Rock Physics Handbook,* Cambridge Univ. Press.

McDonal, F.J., Angona, F.A., Milss, R.L., Sengbush, R.L., Van Nostrand, R.G. & White, J.E., 1958. Attenuation of shear and compressional waves in Pierre shale, *Geophysics,* **23,** 421–439.

Missiaen, T., Versteeg, W. & Henriet, J.P., 2002. A new 3D seismic acquisition system for very high and ultra high resolution shallow water studies, *First Break,* **20,** 227–232.

Neerdael, B., Beaufays, R., Buyens, M., De Bruyn, D. & Voet, M., 1992. Geomechanical behaviour of Boom clay under ambient and elevated temperature conditions, Report EUR 14154 EN.

Piriyakul, K., 2006. Anisotropic stress-strain behaviour of Belgian Boom Clay in the small strain region, *PhD thesis*, University of Ghent.

Stockwell, J.W. & Cohen, J.K., 2008. 'The New SU User's Manual'. Available at: ftp://ftp.cwp.mines.edu/pub/cwpcodes/sumanual-600dpi-a4.pdf (last accessed December 2014).

Thomsen, L., 1986. Weak elastic anisotropy, *Geophysics,* **51,** 1954–1966.

Tsvankin, I., 2012, *Seismic Signatures and Analysis of Reflection Data in Anisotropic Media,* Society of Exploration Geophysicists.

Vandenberghe, N., 1978. *Sedimentology of the Boom Clay (Rupelian) in Belgium*. Verhand. Kon. Acad. Wetensch. Lett. Schone Kunsten van Belgie Klasse Wetensch. Fg XL 1978 nr 147, Paleis der Academiën.

Vanderberghe, N., De Craen, M. & Wouters, L., 2014. *The Boom Clay Geology. From Sedimentation to Present-day Occurrence. A review.* Memoirs of the Geological Survey of Belgium, no. 60, Royal Belgian Institute of Natural Sciences, Geological Survey of Belgium

Vis, G.J. & Verweij, J.M., 2014. Geological and geohydrological characterization of the Boom Clay and its overburden OPERA-PU-TNO411 report.

White, J.E., 1965. *Seismic Waves: Radiation, Transmission and Attenuation,* Mc-Graw Hill.

Wouters, L. & Vandenberghe, N., 1994. *Geologie van de Kempen: Een Synthese,* NIRAS, 208 pp.

Zhan, X, Fang, X., Daneshvar, R., Liu, E. & Harris, C.E., 2014. Full elastic finite-difference modeling and interpretation of karst system in a subsalt carbonate reservoir, *Interpretation,* **2,** T49–T56.

Zhang, F. & Juhlin, C., 2014. Full waveform inversion of seismic reflection data from the Forsmark planned repository for spent nuclear fuel, eastern central Sweden, *Geophys. J. Int.,* **196,** 1106–1122.

APPENDIX A: PIRIYAKUL EQUATIONS AND THOMSEN ANISOTROPY PARAMETERS

Piriyakul's (2006) eq. (2.9) gives the strain–stress relation, whose compliance components are given by

$$s_{11} = \frac{1}{E_h}, \quad s_{12} = -\frac{\nu_{hh}}{E_h}, \quad s_{13} = -\frac{\nu_{vh}}{E_v},$$
$$s_{33} = \frac{1}{E_v}, \quad s_{55} = \frac{1}{G_{hv}}, \quad s_{66} = \frac{2(1+\nu_{hh})}{E_h}, \tag{A1}$$

where $s_{66} = 2(s_{11} - s_{12})$, and E, ν and G denote Young modulus, Poisson ratio and shear modulus, respectively. The subscripts h and v denote horizontal and vertical in that work. The relation between the stiffness and compliance components are

$$c_{11} = \frac{1}{2}\left(\frac{s_{33}}{s} + \frac{1}{s_{11} - s_{12}}\right), \quad c_{12} = \frac{s_{33}}{s} - c_{11}, \quad c_{13} = -\frac{s_{13}}{s},$$
$$c_{33} = \frac{s_{11} + s_{12}}{s}, \quad c_{55} = \frac{1}{s_{55}}, \tag{A2}$$

where

$$s = s_{33}(s_{11} + s_{12}) - 2s_{13}^2$$

(Auld 1990, p. 372).

On the other hand, the anisotropy parameters are

$$\epsilon = \frac{c_{11} - c_{33}}{2c_{33}}, \quad \gamma = \frac{c_{66} - c_{55}}{2c_{55}}, \quad \delta = \frac{(c_{13} + c_{55})^2 - (c_{33} - c_{55})^2}{2c_{33}(c_{33} - c_{55})} \tag{A3}$$

(Thomsen 1986).

APPENDIX B: RAY TRACING IN ANISOTROPIC MEDIA

In TI media, the formulation of the non-hyperbolic reflection moveout of P-waves proposed by Alkhalifah & Tsvankin (1995) is quite appropriate to model arrival times in seismic experiments. Consequently, the same formulation can be used to invert picked traveltimes for the Thomsen anisotropy parameters (Thomsen 1986; Gei *et al.* 2011).

Fig. 3(a) shows a typical RVSP scheme of acquisition of seismic data, where $t(0)$ and $t(x)$ are the zero offset one-way traveltime and the traveltime to the receiver located at distance x from the well-head, respectively, for both P- and S-waves.

In laterally homogeneous VTI media, the traveltime of the qP wave can be approximated by (Alkhalifah & Tsvankin 1995),

$$t_{\rm P}^2(x) = t_{\rm P}^2(0) + \frac{x^2}{v_{\rm NMO}^2} - \frac{2\eta x^4}{v_{\rm NMO}^2[t_{\rm P}^2(0)v_{\rm NMO}^2 + (1+2\eta)x^2]}, \tag{B1}$$

where $t_{\rm P}(0)$ is the is the zero offset P-waves one-way traveltime, x is the offset, that is, the horizontal projection of the source–receiver distance and $v_{\rm NMO}$ is the normal moveout velocity, which in the case of anisotropic media is given by

$$v_{\rm NMO} = v_{\rm P0}\sqrt{1+2\delta}, \tag{B2}$$

where $v_{\rm P0}$ is the P-wave velocity measured along the vertical symmetry and η is the anellipticity

$$\eta = \frac{\epsilon - \delta}{1 + 2\delta}, \tag{B3}$$

ϵ and δ are two of the three Thomsen anisotropy parameters. The inversion algorithm consists in a nonlinear iterative minimization of the residual traveltimes given by the difference between the synthetic traveltimes computed with eq. (B1) and experimental traveltimes. The latter are given by

$$t_{\rm P}(x) = t_{\rm P}^a - t_0, \tag{B4}$$

where $t_{\rm P}^a$ are the observed arrival times and t_0 is the, generally unknown, origin time.

APPENDIX C: STABILITY CONDITIONS OF A TI MEDIUM

The stability condition of a TI medium is

$$c_{11} > |c_{12}|, \quad (c_{11} + c_{12})c_{33} > 2c_{13}^2, \quad c_{55} > 0 \tag{C1}$$

(Carcione 2015). In the isotropic case this becomes

$$c_{11} > |\lambda|, \quad \lambda + \frac{2}{3}\mu > 0, \quad \mu > 0, \tag{C2}$$

where $c_{11} = \lambda + 2\mu$ and λ and μ are the Lamé constants.

Note that for a TI medium, we have

$$c_{13} = \sqrt{2\delta c_{33}(c_{33} - c_{55}) + (c_{33} - c_{55})^2} - c_{55}. \tag{C3}$$

APPENDIX D: CALCULATION OF THE DILATATION QUALITY FACTOR

The P-wave quality factor is given by

$$Q_P = \frac{{\rm Re}(\bar{v}_P^2)}{{\rm Im}(\bar{v}_P^2)},$$

$$\rho\bar{v}_P^2 = KM_1 + \frac{4}{3}\mu M_2 = \rho\left[\left(v_P^2 - \frac{4}{3}v_S^2\right)M_1 + \frac{4}{3}v_S^2 M_2\right], \tag{D1}$$

where $\bar{v}_P$ is the complex P-wave velocity, M_1 and M_2 are complex moduli, while

$$Q_K = \frac{\mathrm{Re}(\bar{K})}{\mathrm{Im}(\bar{K})}, \quad \bar{K} = KM_1 = \rho\left(v_P^2 - \frac{4}{3}v_S^2\right)M_1 \tag{D2}$$

and

$$Q_S = \frac{\mathrm{Re}(M_2)}{\mathrm{Im}(M_2)} \tag{D3}$$

(Carcione 2015).

It is $Q_1 = Q_K$ at the centre frequency of the relaxation peak.

APPENDIX E: WAVE VELOCITIES AND QUALITY FACTORS

The complex velocities are required to calculate wave velocities and quality factors of the medium. They are given by

$$v_{\mathrm{qP}} = (2\rho)^{-1/2}\sqrt{p_{11}l_1^2 + p_{33}l_3^2 + p_{55} + A}$$

$$v_{\mathrm{qSV}} = (2\rho)^{-1/2}\sqrt{p_{11}l_1^2 + p_{33}l_3^2 + p_{55} - A}$$

$$v_{\mathrm{SH}} = \rho^{-1/2}\sqrt{p_{66}l_1^2 + p_{55}l_3^2}$$

$$A = \sqrt{[(p_{11} - p_{55})l_1^2 + (p_{55} - p_{33})l_3^2]^2 + 4[(p_{13} + p_{55})l_1l_3]^2} \tag{E1}$$

(Carcione 2015), where $l_1 = \sin\theta$ and $l_3 = \cos\theta$ are the directions cosines, θ is the propagation angle between the wavenumber vector and the symmetry axis, and the three velocities correspond to the *qP*, *qS* and *SH* waves, respectively. The phase velocity is given by

$$v_p = \left[\mathrm{Re}\left(\frac{1}{v}\right)\right]^{-1}, \tag{E2}$$

where v represents either v_{qP}, v_{qSV} or v_{SH}. The energy-velocity vector of the *qP* and *qSV* waves is given by

$$\frac{\mathbf{v}_e}{v_p} = (l_1 + l_3\cot\psi)^{-1}\hat{\mathbf{e}}_1 + (l_1\tan\psi + l_3)^{-1}\hat{\mathbf{e}}_3 \tag{E3}$$

(Carcione 2015), where

$$\tan\psi = \frac{\mathrm{Re}(\beta^* X + \xi^* W)}{\mathrm{Re}(\beta^* W + \xi^* Z)}, \tag{E4}$$

defines the angle between the energy-velocity vector and the z-axis (the ray angle),

$$\beta = \sqrt{A \pm B},$$

$$\xi = \pm \mathrm{pv}\sqrt{A \mp B},$$

$$B = p_{11}l_1^2 - p_{33}l_3^2 + p_{55}\cos 2\theta, \tag{E5}$$

where the upper and lower signs correspond to the *qP* and *qS* waves, respectively. Moreover,

$$W = p_{55}(\xi l_1 + \beta l_3),$$

$$X = \beta p_{11}l_1 + \xi p_{13}l_3,$$

$$Z = \beta p_{13}l_1 + \xi p_{33}l_3 \tag{E6}$$

(Carcione 2015), where 'pv' denotes the principal value, which has to be chosen according to established criteria.

On the other hand, the energy velocity of the *SH* wave is

$$\mathbf{v}_e = \frac{v_p}{\rho\mathrm{Re}(v)}\left[l_1\mathrm{Re}\left(\frac{p_{66}}{v}\right)\hat{\mathbf{e}}_1 + l_3\mathrm{Re}\left(\frac{p_{55}}{v}\right)\hat{\mathbf{e}}_3\right]. \tag{E7}$$

Finally, the attenuation and quality factors are given by

$$\alpha = -\omega\mathrm{Im}\left(\frac{1}{v}\right) \tag{E8}$$

and

$$Q = \frac{\mathrm{Re}(v^2)}{\mathrm{Im}(v^2)}, \tag{E9}$$

respectively.

APPENDIX F: REFLECTION COEFFICIENT OF A LAYER

The scattering coefficients for a layer can be found in Carcione (2015). For an incidence wave with subscript W = P or W = S, where P and S denote compressional and shear waves, the reflection-transmission coefficient vector is

$$[R_{\mathrm{WP}}, R_{\mathrm{WS}}, T_{\mathrm{WP}}, T_{\mathrm{WS}}]^\top = (\mathbf{B}\mathbf{A}_2 - \mathbf{A}_1)^{-1}\,\mathbf{i}_W, \tag{F1}$$

where $\mathbf{A}_1$ and $\mathbf{A}_2$ are the propagator matrices related to the upper and lower media, $\mathbf{B}$ is the propagator matrix of the layer, and $\mathbf{i}_W$ is the incidence vector. The explicit expressions can be found in Carcione (2015; chapter 6).

In many works, an approximate simple expression of the reflection coefficient of a single layer, neglecting the shear waves, is used. Referring to Fig. 15, the solution is given by

$$R = \frac{r\,[1 - \exp(-\beta)]}{1 - r^2\exp(-\beta)}, \tag{F2}$$

where

$$\beta = 2\mathrm{i}h\left(\frac{\omega}{\bar{v}_{P2}}\right)\cos\theta_2, \tag{F3}$$

$$r = \frac{Z_2\cos\theta_1 - Z_1\cos\theta_2}{Z_2\cos\theta_1 + Z_1\cos\theta_2}, \quad Z_j = \rho_j\bar{v}_{Pj}, \quad j = 1, 2 \tag{F4}$$

where h is the thickness of the layer, Z is the impedance, and Snell's law is $\sin\theta_1/\bar{v}_{P1} = \sin\theta_2/\bar{v}_{P2}$. Eq. (F4) is a generalization to the viscoelastic case, since $\bar{v}_P$ is a complex velocity.

The absolute value of the PP-reflection coefficient at normal incidence is given by

$$R_{\mathrm{PP}}(0) = \frac{2|R_0\sin(kh)|}{|R_0^2\exp(-\mathrm{i}kh) - \exp(\mathrm{i}kh)|} \tag{F5}$$

(Carcione 2015), where $k = \omega/v_{P2}$ and

$$R_0 = \frac{Z_2 - Z_1}{Z_2 + Z_1}.$$

It is clear from eq. (F5) that the reflection coefficient vanishes for $h = nv_{P2}/(2f)$, $n = 1, 2, 3, \ldots$

APPENDIX G: RICKER WAVELET USED IN THE SIMULATIONS

The Ricker time history used in the simulations is

$$w(t) = \left(a - \frac{1}{2}\right)\exp(-a), \quad a = \left[\frac{\pi(t - t_s)}{t_p}\right]^2, \tag{G1}$$

where t_p is the period of the wave (the distance between the side peaks is $\sqrt{6}t_p/\pi$) and we take $t_s = 1.4t_p$. Its frequency spectrum is

$$W(\omega) = \left(\frac{t_p}{\sqrt{\pi}}\right)\bar{a}\exp(-\bar{a} - \mathrm{i}\omega t_s), \quad \bar{a} = \left(\frac{\omega}{\omega_p}\right)^2, \quad \omega_p = \frac{2\pi}{t_p}. \tag{G2}$$

The peak frequency is $f_p = 1/t_p$.